TERAHERTZ IMAGING FROM PROJECTIONS USING A PARALLEL PLATE WAVEGUIDE APERTURE IN TRANSMISSION AND REFLECTION MODE

By

MOHAMMAD MA'MOUN AWAD

Bachelor of Science

Oklahoma State University

Stillwater, USA

2001

Submitted to the Faculty of the
Graduate College of the
Oklahoma State University
in partial fulfillment of
the requirements for
the Degree of
MASTERS OF SCIENCE
May, 2005

TERAHERTZ IMAGING FROM PROJECTIONS

USING A PARALLEL PLATE WAVEGUIDE

APERTURE IN TRANSMISSION AND

REFLECTION MODE

Thesis Approved:

Dr.Alan Cheville
Thesis Advisor

Dr. Daniel Grischkowsky

Dr. Charles Bunting

Dr. Gordon Emslie
Dean of Graduate College

Acknowledgements

I would like to express my sincere gratitude to my academic advisor, Dr. Alan Cheville, for giving me the opportunity to be a member of his research group, and for his guidance and support throughout this endeavor. I also would like to thank my committee members Dr. Daniel Grischkowsky and Dr. Charles Bunting for their time and advice.

My thanks also to Ali, friend extraordinaire, and Loay who both provided the much needed relief from the day-to-day activities of a graduate student. To both of you good luck!

Finally, I cannot thank my parents enough for all their love and support throughout the years, and most importantly for their never ending patience and encouragement. To Nour, Zaid, Hamzah and Gounwa thanks for your patience and understanding for what was a long time away from home.

-*Mohammad M. Awad*

April, 2005

Table of Contents

List of Tables

List of Figures

List of Symbols

$\alpha(z)$	Absorption
b	Parallel plate waveguide spacing
δ	Impulse function
δ_s	Skin depth, m
D	Frequency scaling parameter
$E(y)$	Electric field amplitude in y-direction
$E_{Ref}(t)$	Time resolved electric field of a reference scan
$E_{Sample}(t)$	Time resolved electric field of a sample scan
f	Frequency, Hz
$f(x,y)$	Image density function
$F(\xi_x,\xi_y)$	2-dimensional Fourier Transform
$F_P(\xi,\theta)$	Fourier transform in polar coordinates
FDTD	Finite Difference-Time Domain
FWHM	Full Width Half Maximum
$g(s,\theta)$	Radon transform of f(x,y)
GaAs	Gallium Arsenide
$G(\xi,\theta)$	Radon transform in freqency domain
GVD	Group Velocity Dispersion
KLM	Kerr lens mode-locked
m,n	Mode indicies
s	Rotated x-axis
t	Time, s
θ	Angle of rotated coordinate system (u,s)

TE	Transverse Electric
TEM	Transverse Electromagnetic
TM	Transverse Magnetic
$I(l, \omega)$	Frequency dependent beam-profile along the aperture
Γ	Reflection Coefficient
$\mathcal{F}$	Fourier Transform
$\mathcal{F}^{-1}$	Inverser Fourier Transform
$\mathcal{B}$	Backprojection Operator
$\mathcal{R}$	Radon Transform Operator
ξ	Variable in Fourier space
Δz	Sample Thickness, m
ω	Angular frequency, rad/s
λ	Wavelength, m
x, y, z	Cartesian coordinates
Z_R	Confocal distance
f_{cyl}	Focal length of cylindrical lens
THz-TDS	Terahertz Time Domain Spectroscopy
SOS	Silicon-on-Sapphire
TM_0	Zero order Transverse magnetic mode
$H(\omega)$	Complex Transfer Function
PSF	Pointspread Function
V_{DC}	DC Voltage
$w(z)$	Beam radius at z, m
w_o	Beam waist radius, m

Chapter 1
Introduction

The terahertz frequency range lies in between the microwave and optical regimes. This frequency range until recently, has not been easily accessible due to the lack of means to efficiently generate and detect it. However, this has changed in recent years, with different technologies available to generate and detect THz radiation. As a result there has been a surge of applications being demonstrated at THz frequencies. Among these applications are material characterization [1, 2], spectroscopy [3, 4, 5, 6], imaging [7, 8, 9], sensing [10] and ranging applications [11, 12].

Recently, THz imaging has seen several new developments. Since the first THz image was produced, many different approaches and imaging techniques have been explored and demonstrated. Especially in the medical field, there have been several studies utilizing THz radiation to identify basal cell carcinoma in human skin tissue [13, 14, 15] and compared to X-rays for example, THz radiation is non-ionizing, having energies of approximately 4meV at 1THz. This makes it especially attractive for medical purposes, however the relatively large wavelength, $300\mu m$ at 1THz, limits the imaging resolution at THz frequencies.

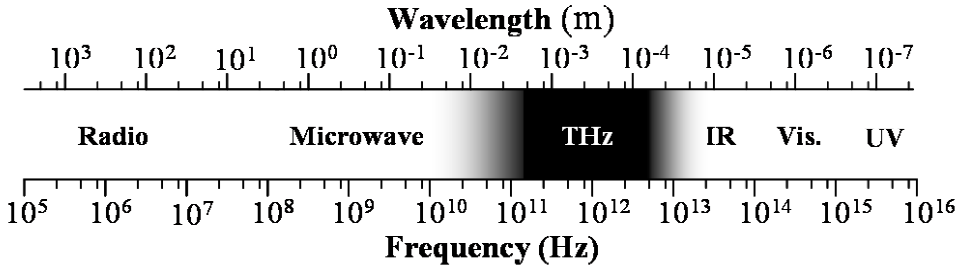

Figure 1.1: Electromagnetic Spectrum

1.1 THz Imaging Techniques

Following is a short overview of several THz imaging techniques, which relate to the experimental work described in this document.

1.1.1 Raster Scan

The raster scan method was the first type of imaging method demonstrated [7] in the THz frequency range. A focused THz beam system was used as an imaging setup. The imaging target was mounted on a xy translation stage and placed at the focal plane and each pixel was acquired individually by moving the target across the beam focus. The image data was collected using a optical scanning delay line. Since complete time resolved scans were obtained, it was possible to detect the chemical composition of the target. To demonstrate the this type of chemical composition detection, the hydration level of a tree leaf was measured twice. The measurements were separated by 48 hours and the image taken after 48 hours showed significantly less absorption of the incident THz radiation. The resolution of this technique is limited by the diffraction limit of the optics used to focus the THz beam and was approximately $400\mu m$. A 300×300 pixel image requires the acquisition of $90{\cdot}10^3$ data-points which

makes imaging of large targets impractical.

1.1.2 Tomographic Imaging

Several different tomographic imaging techniques have been applied at the THz frequency range. Time of flight data in a reflection geometry is used to map reflections from different interfaces to depth information. This technique has been used to reconstruct a cross section of a 3.5" floppy disk [16]. Also computed tomography (CT) was demonstrated using a focused beam system. The target was mounted on a rotation stage and positioned at the beam focus. To acquire an image, the target is rotated and the measured projections used to reconstruct the an image. This method is used in x-ray computed tomography and can be used to acquire a three dimensional model of an object.

1.1.3 Near-field Aperture Imaging

To achieve sub-wavelength resolution, it is possible to pass the illuminating radiation through a sub-wavelength aperture. Near-field aperture imaging has been achieved by coupling THz radiation into a tapered tube aperture. The aperture is in close contact with the imaging target and the image is acquired by raster scanning the target across the the aperture. The limit of resolution in this case is established by the aperture size [17]. An imaging resolution of $\frac{\lambda}{4}$ were achieved using this method.

1.1.4 Scanning Probe Tip

Sub-micron resolution is achieved using a scanning probe tip, [18]. The focused THz pulse is reflected off the target surface at 70^o while a metal tip is placed above the image point. Incident THz radiation induces a dipole moment in the probe tip that leads to partial absorption and scattering of the THz radiation. The remaining THz radiation is then detected and measured. Using this technique, spatial resolution of 150nm has been achieved.

1.1.5 THz Imaging from Projections

The imaging method described in this document,THz imaging from projections, is used in conjunction with two apertures:

- Conventional silicon lens aperture
- Near-field parallel plate waveguide aperture

Unlike raster scan techniques, projection type imaging techniques acquire data in the form of the radon transform, and reconstruction algorithms have to be used to extract the image. The radon transform and an inversion algorithm is discussed in chapter 4. The silicon lens aperture is used to acquire an image limited in its resolution by the diffraction limit of the optics. The near-field parallel plate waveguide aperture produces images with a resolution set by the spacing of the waveguide walls. Both apertures are discussed in-depth in chapter 3. Furthermore, two imaging geometries are considered for both apertures: transmission mode and reflection mode, which are described in chapter 5. The type of samples that can be imaged in a transmission geometry are limited, specially when considering biological samples or

samples with large absorption along the axis of propagation. In reflection mode however, this imaging method may be of interest in investigating a much larger range of samples. Using the imaging from projections technique, we demonstrate imaging at a resolution limited by the diffraction limit of conventional optics, and sub-wavelength resolution using the near-field properties of a parallel plate waveguide. This type of imaging technique using both apertures and geometries is novel at THz frequencies. Using a waveguide to achieve sub-wavelength resolution however has been previously demonstrated at millimeter wavelengths to measure spatio-temporal carrier relaxation in silicon in a transmission and reflection geometry [19, 20]. These measurements were done acquiring scattering parameters, and the experimental setup differs largely from the experimental setup used at THz frequencies. The following chapter describes a standard THz setup and how THz radiation is generated and detected.

Chapter 2
THz-TDS System Description

The standard terahertz time-domain spectroscopy (THz-TDS) system shown in figure 2.1 is the basis of a majority of THz applications, and the transmission imaging configuration is built upon it. A complete THz-TDS [21] system consists of a THz transmitter, beam collecting and steering optics and a THz receiver. THz radiation is generated by photoconductive switching of the transmitter. The receiver is time-gated by a delayed optical pulse; by varying the relative time delay between the THz radiation incident upon the receiver and the gating optical pulse it is possible to map the detected electric field as a function of relative time-delay. This chapter briefly describes each of the individual components in a THz-TDS system.

2.1 Optics

Figure 2.1 shows a schematic of a standard THZ-TDS system. A nominally frequency independent beam waist, w_1, is created at the surface of the spherical lens on the THz transmitter side. The off-axis paraboloidal mirror (OAPM) collimates the THz beam creating a frequency dependent beam waist at w_2 which is also a plane of symmetry for the system. The focal length of the OAPMs is $f = 119mm$. A second OAPM focuses the THz beam onto the receiver. The two OAPMs are in a confocal configuration, separated by twice their focal length ($2f$). To acquire fully time resolved scans, it is

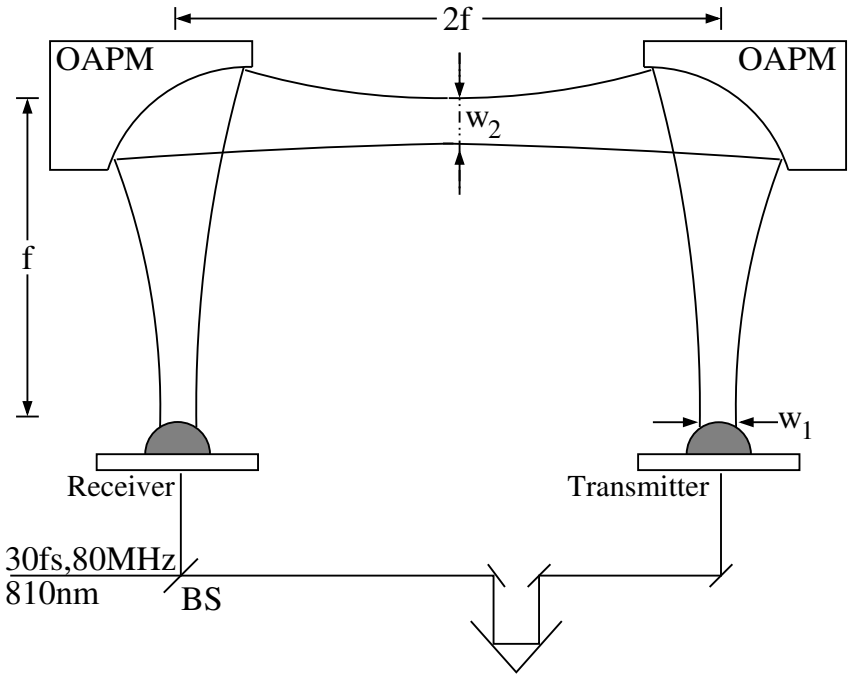

Figure 2.1: A Standard THZ-TDS System

necessary to vary the relative time delay between the incident THz radiation and the optical pulse gating the THz receiver. This relative time delay between the incident THz radiation and receiver gating pulse is usually accomplished using a a beam-splitter to partially reflect some of the optical excitation onto the receiver and transmit the remainder onto the transmitter via an optical delay line. The optical delay line is simply two mirrors mounted orthogonally to each other,acting as a retroreflector and set on a translation stage. Moving the delay line maps out the receiver photocurrent as a function of relative time delay between the incident THz radiation and receiver gating pulse. A typical THz-TDS measurement is performed by taking two separate scans. One scan is performed without any sample and is called the reference scan. A second scan, called sample scan, is made with the sample placed at w_2. Now the

transfer function can be evaluated numerically as:

$$H(\omega) = \frac{E_{Sample}(\omega)}{E_{Reference}(\omega)} \tag{2.1}$$

where $E_{Sample}(\omega)$ and $E_{Reference}(\omega)$ are the numerical Fourier transforms of the respective acquired time-resolved signals. Due to the high absorption of water vapor in the THz frequency range [22], the experiment has to be purged with dry air.

2.2 THz Generation and Detection

2.2.1 Transmitter

The terahertz transmitter used to generate THz radiation is a set of two coplanar $20\mu m$ transmission lines separated by $80\mu m$ that are fabricated on semi-insulating (SI) gallium arsenide (GaAs) [23, 24], shown in figure 2.2(a). The transmission lines are biased at $80V_{DC}$. Carriers are generated in the semiconductor by photo-excitation from a Kerr lens mode-locked (KLM) Ti:Sapphire laser focused close to the anode and operating at a center wavelength of $810nm$ with a pulse repetition rate of approximately 80MHz and a $30fs$ pulse width. The optically generated carriers are accelerated by the electric field created by the DC bias, resulting in the generation of THz radiation. SI GaAs has a long carrier lifetime, which means that the majority of carriers contribute to the generation of THz radiation instead of recombining. The generated THz radiation is then coupled out of the backside of the semiconductor by means of a spherical high resistivity silicon lens. To efficiently collect the generated THz radiation, the height of the lens has to be such that the lens focus lies at the front side of the chip.

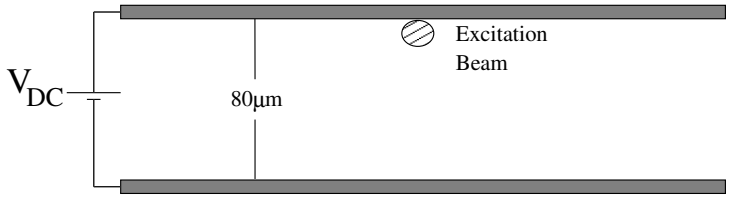

(a) THz Transmitter

(b) THz Receiver

Figure 2.2: THz Transmitter and Receiver

2.2.2 Receiver

The THz receiver is a dipole antenna structure fabricated on an ion-implanted [25] silicon-on-sapphire (SOS) substrate. The transmission lines are $30\mu m$ wide, the dipole is $20\mu m$ wide with a $5\mu m$ gap in between, see figure 2.2(b). The THz receiver is connected to a variable gain low-noise current amplifier set to a transconductance of $10^{-7}\frac{A}{V}$. Depending on the type of data acquisition performed, the output of the current amplifier is either connected to a lock-in amplifier, or to a bandpass filter and amplifier. The data acquisition is further discussed in a separate section.

2.3 Data Acquisition

The previous sections describe the generation, steering and detection of THz radiation which ended at the low-noise current amplifier. The output voltage from the current amplifier has to be filtered and stored by the data acquisition system. The data acquisition system has to perform two tasks at a minimum:

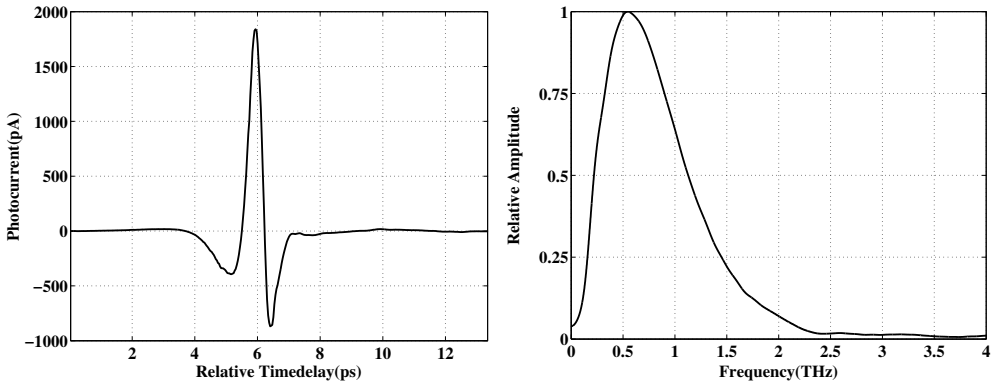

(a) THz Pulse (b) Frequency Spectrum

Figure 2.3: THz Pulse and corresponding Frequency Spectrum

1. Control the delay line

2. Record voltage from the current amplifier

In addition to those tasks, the data acquisition system has to control other mechanics used for sample translation. A full description of the sample mounting and translation mechanics for this experiment can be found in chapter 5.

The output voltage from the current amplifier is detected in two different ways:

2.3.1 Lock-in Detection

A lock-in amplifier requires the use of a mechanical chopper to modulate the transmitted THz beam. The chopper electronics also provides a reference signal for the lock-in amplifier, and only a signal at the same frequency as the reference signal is detected. Lock-in detection allows for very high signal-to-noise ratios in excess of 10,000:1 [21]. Figure 2.3 shows a THz pulse and its corresponding frequency spectrum. Typically, a time resolved scan is acquired using a computer controlled optical delay line. A single data point is collected and the delay line advanced, however it is

not feasible to acquire fully time resolved scans for a complete image considering the time it takes to complete a full scan. The long data acquisition time is due to the relatively long time constant, τ, and the associated settling time of $3 \cdot \tau$ associated with it. Therefore, for all image data that were collected using a lock-in amplifier, only the peak of the signal was acquired. Practically this means, that the optical delay line was adjusted to coincide with the peak of the THz pulse, and changes only due to the sample movement were acquired. This technique assumes that the sample does not incur any changes in timing. This method does not retain any spectral information from the data scans. The lock-in amplifier and motion controller are connected to a PC using a GPIB interface to automate the data acquisition process.

2.3.2 Rapid Scanning Delay Line

Using this method, the lock-in amplifier and mechanical chopper are replaced with an amplifying bandpass-filter which is connected to the data-acquisition hardware. Also, to accomplish a fast scanning delay, a retroreflector is mounted on a speaker. The speaker is driven by a 17Hz sine wave, which also supplied the trigger for the data acquisition computer. The movement of the speaker provides a relative time delay of approximately $80ps$. This type of delay line allows for much faster data acquisition, at the cost of a lower signal to noise ratio. Every time the data acquisition computer is triggered, it collects a set amount of points at a given sampling rate. Several scans are acquired and averaged to improve the SNR.

Both above methods are used to collect the image data used in this experiment. As for time consideration, both methods approximately required the same amount

of time to acquire an image. However the amount of data collected using the rapid scanning delay line is about 40MB/Image whereas using a lock-in amplifier the size of the data did not exceed 150kb/Image. However it is important to remember that there is potentially usable information contained in full time resolved data that is never recorded using non-time resolved lock-in detection.

The next chapter describes the imaging apertures used to image the target and discusses the properties of the THz beam and its effect on image resolution.

Chapter 3
Imaging Apertures

Two different types of apertures are used to image the target in both geometries, transmission and reflection. To establish the limit of resolution for conventional silicon optics, a set of identical cylindrical lenses in a confocal configuration was used to image the target. Second, the same cylindrical lenses were used to couple the THz radiation in and out of a parallel plate waveguide with a plate spacing of $100\mu m$. The output face of the waveguide serves as the waveguide imaging aperture and the sample is sandwiched between the waveguide and the coupling cylindrical lens. This chapter describes the imaging optics used, the characteristics of the illumination and its effect on image resolution. The cylindrical lens is referred to as an imaging aperture throughout this document, however it is important to point out the difference between it and the waveguide aperture. Unlike the parallel plate waveguide aperture, which is an actual physical aperture, the cylindrical lens "soft" aperture is defined by the characteristics of the Gaussian beam at its focus.

3.1 Effect of an Aperture on Image

A point source, imaged by some optical system, does not reproduce as a point in the image plane, but rather as a finite distribution. This is due to aberrations in the optical system. A design of an optical system that accounts and corrects the

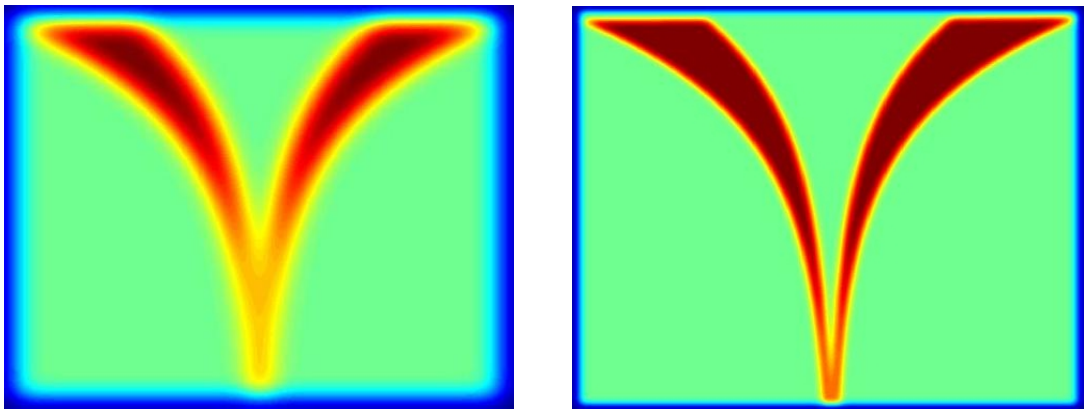

(a) Cylindrical Lens (b) Waveguide Aperture

Figure 3.1: Target convolved with Gaussian

aberrations is said to be diffraction limited. The diffraction limit is defined later in this chapter. Mathematically, the effects of an optical system on an object function $f(x, y)$ can be calculated from 3.1, where $\otimes$ is the convolution operation, $h(x, y)$ impulse response or point-spread function of the system, and f'(x,y) the image.

$$f'(x, y) = h(x, y) \otimes f(x, y) = \int_{-\infty}^{\infty} \int_{-\infty}^{\infty} h(x - x', y - y') f(x', y') dx' dy' \qquad (3.1)$$

The point-spread function includes the complete response of the system, which in this case includes the response of the backprojection operation and that of the actual imaging optics whether in transmission or reflection mode. The effect of the point-spread function of the backprojection operation however is minimal when compared to the spatial extent of the illumination, and the resulting image depends mainly on the optics used. Figures 3.1(a) and (b) show the 2-dimensional convolution of the target image with a Gaussian of the size generated by the respective apertures.

As shown in the next chapter, it is necessary for the illuminating beam to have a high aspect ratio. This is accomplished by using a cylindrical lens which creates an

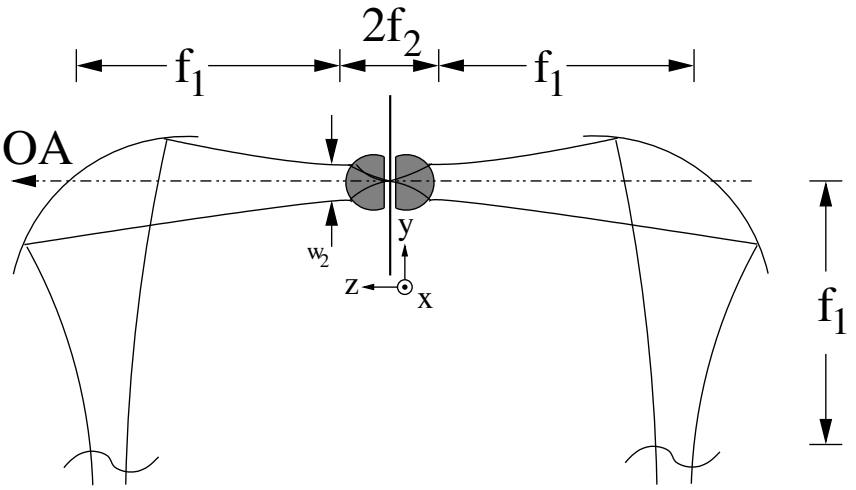

Figure 3.2: Confocal Cylindrical Lens Configuration

elliptical focus, however the minimal focused spot size is limited by the diffraction limit of the optics. Using the near-field properties of a parallel plate waveguide with a plate spacing less than a wavelength, it is possible to create a high brightness, sub-wavelength line source. This type of aperture allows for imaging with sub-wavelength resolution.

3.2 Cylindrical Lens Aperture

The images obtained from the cylindrical lens set the basis for comparison with the parallel plate waveguide aperture images. The cylindrical lenses are also used to couple in and out of the waveguide, however the limit of resolution in this case is the waveguide plate spacing rather than the diffraction limit of the optics. The geometry of the cylindrical lens is shown in figure 3.3 where h=6.55mm, d=10mm, r=5mm, ht=15mm. The lenses are manufactured from high resistivity silicon, which has high transparency and very low dispersion at THz frequencies.

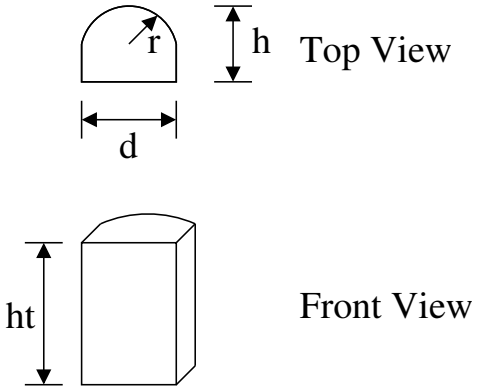

Figure 3.3: Cylindrical Lens

In the transmission mode configuration, two cylindrical lenses, spaced by the sum of their focal lengths, are placed at the system beam waist, shown in figure 3.2. Focusing using a cylindrical lens only occurs in the plane of curvature of the lens or the zy-plane in figure 3.2, the beam profile along the x-direction however remains in the form of a collimated frequency dependent Gaussian. Since the THz beam has a quasi-Gaussian beam profile [26, 24, 27], the beam radius at the focal plane in the y-direction can be expressed as:

$$w = w_{minor} \approx \frac{\lambda f_{cyl}}{\pi w(\lambda)} \tag{3.2}$$

where λ is the free space wavelength, f_{cyl} is the focal length of the cylindrical lens and $w(\lambda)$ is the frequency dependent beam entering the lens. The resulting THz beam profile has an elliptical shape with the calculated w_{major} and w_{minor} at $0.6THz$ equal to $15.2mm$ and $300\mu m$ respectively at $0.6THz$. The resolution is established by w_{minor}.

3.3 Parallel Plate Waveguide Aperture

The cylindrical lenses, as any conventional optical elements, are limited in their imaging resolution by the diffraction limit. The near-field characteristics of the parallel plate waveguide however allow for imaging with a resolution at a fraction of a wavelength. The resolution achievable using this method is approximately equal to the waveguide plate separation or slit width [20, 28]. Generally, radiation propagating through sub-wavelength apertures undergoes high attenuation, this is not the case with parallel plate waveguides. A parallel plate waveguide has no inherent mode cutoff as the plate spacing is decreased. Also it allows for near dispersion-free propagation of THz pulses with losses primarily determined by the overlap of the THz free-space electric field and the waveguide mode [29].

3.3.1 Waveguide Modes

The incident THz radiation is linearly polarized in the direction orthogonal to the waveguide plates. The same high resistivity-silicon cylindrical lenses used as imaging apertures now couple this radiation into a TM_0 mode, which is TEM mode. The spatial dependence of E_y is shown from equation 3.3 to be $cos(\frac{n\pi}{b}y)$. This relation is plotted in figure 3.4.

The following equations describe the electric and magnetic fields for TM propagating modes [30]:

$$E_y = -B_n \frac{n\pi\beta_z}{b\omega\mu\epsilon} cos\left(\frac{n\pi}{b}y\right) e^{-\jmath\beta_z z} \tag{3.3}$$

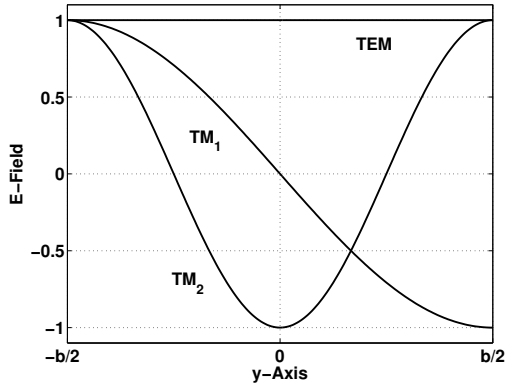

Figure 3.4: Mode profiles of the first 3 TM modes

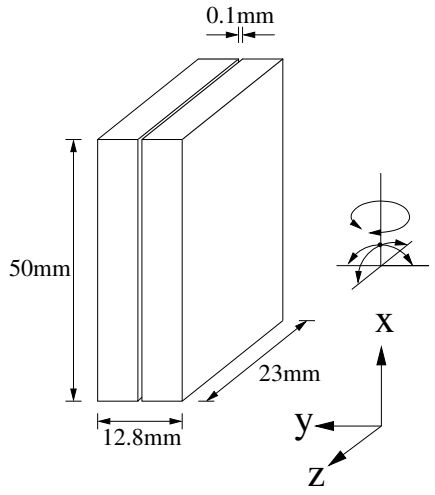

Figure 3.5: Parallel Plate Waveguide

3.3.2 Waveguide Construction

The THz waveguide is constructed from two optically polished brass slabs separated by $100\mu m$ spacers, see figure 3.5. The inside walls of the waveguide are gold plated. The waveguide is mounted on a tip-tilt and rotation stage to allow for alignment with the coupling optics and sample.

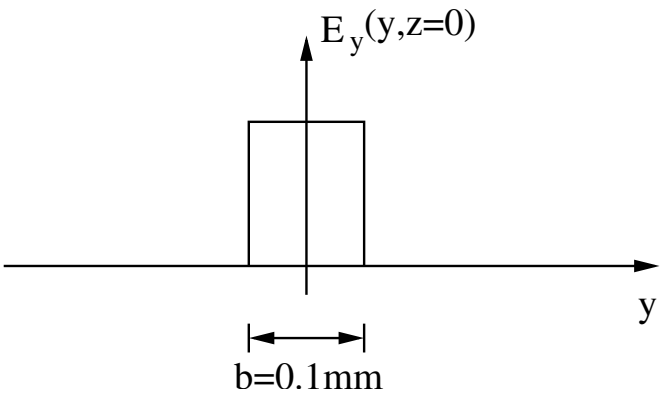

Figure 3.6: Electric field at the output face of the waveguide

3.3.3 Diffraction from Single Slit Aperture

Before treating the effect of diffraction at the aperture for propagating modes, it is necessary to look at the angular spectrum at the exit slit of the waveguide. Since the aperture does not have any resolution along the x-direction, the problem is reduced to two variables, i.e. the yz-plane, figure 3.5.

The following treatment is an adaptation from [31] into the cross-sectional dimension of the waveguide along the y-axis. The angular spectrum of the electric field at the output of the waveguide($z = 0$) is given as:

$$A(\xi_y, z = 0) = \int_{-\infty}^{\infty} E(y, 0) \cdot e^{-j2\pi(\xi_y y)} dy \tag{3.4}$$

where $E_y(y, z = 0)$ is a nearly one dimensional field distribution across the waveguide plates shown in figure 3.6. and the electric field can be expressed in terms of its spectral components as:

$$E(y, z = 0) = \int_{-\infty}^{\infty} A(\xi_y, 0) \cdot e^{j2\pi(\xi_y y)} d\xi_y \tag{3.5}$$

Also, $E(y, z)$ has to satisfy the Helmholtz equation which means A has to satisfy

the propagation relation [31]:

$$A\left(\frac{\alpha}{\lambda},\frac{\beta}{\lambda},z\right)=A\left(\frac{\alpha}{\lambda},\frac{\beta}{\lambda},0\right)\cdot e^{\left(\jmath\frac{2\pi}{\lambda}\cdot\sqrt{1-\alpha^2-\beta^2}\cdot z\right)} \tag{3.6}$$

where λ is the wavelength and $\alpha=\lambda\xi_x$, $\beta=\lambda\xi_y$ and $\gamma=\sqrt{1-\alpha^2-\beta^2}$ are the direction cosines of a plane wave, as defined in figure 3.7. For propagation in the yz-plane, $\alpha=0$. If $1-\beta^2<0$ then

$$\beta=\xi_y\lambda>1 \text{ and } \lambda>\frac{1}{\xi_y} \tag{3.7}$$

For frequency components for which equation 3.7 holds true, the radiation is non-propagating or evanescent and decays exponentially as the distance from the aperture increases:

$$A\left(\frac{\beta}{\lambda},z\right)=A\left(\frac{\beta}{\lambda},0\right)\cdot e^{-\frac{2\pi}{\lambda}\sqrt{\beta^2-1}\cdot z} \tag{3.8}$$

Limiting the case to the yz-plane, the measured electric field amplitude can be written as:

$$E_t(y,z=0)=f(x_o,y)\cdot E_i(y,z=0) \tag{3.9}$$

where E_t and E_i are the transmitted and incident electric field amplitude respectively. $f(x_o,y)$ is the image density function or amplitude transmittance function along a line normal to the aperture and intersecting the x-axis at x_o. Taking the Fourier transform of equation 3.9 and using the convolution theorem yields [31]:

$$A_t\left(\frac{\beta}{\lambda}\right)=A_i\left(\frac{\beta}{\lambda}\right)\otimes T\left(\frac{\beta}{\lambda}\right) \tag{3.10}$$

where

$$T\left(\frac{\beta}{\lambda}\right)=\int_{-\infty}^{\infty} f(x_o,y)\cdot e^{-2\jmath\pi\left(\frac{\beta}{\lambda}y\right)}dy \tag{3.11}$$

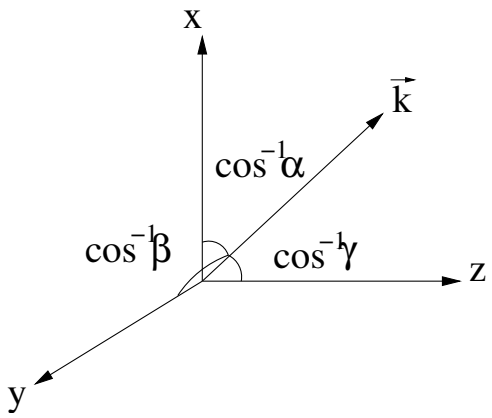

Figure 3.7: Direction cosines

Equation 3.8 shows that to achieve sub-wavelength resolution, it is necessary to get the target into close contact with the aperture. The distance between the target and the waveguide aperture was measured to be approximately $25\mu m$. This distance was measure by fitting precision metal sheets between the aperture and the target.

Once the radiation exits the aperture, it spreads rapidly due to the sub-wavelength confinement of the waveguide. This spreading affects the resolution of the aperture. Thus, the target-waveguide spacing has a two fold negative effect on the image quality. As the distance increases, the SNR decreases and also the resolution.

The near-field diffraction pattern from a single slit is evaluated numerically using the convolution form of the Fresnel diffraction integral [31], shown in figure 3.8 [31] where the aperture size is indicated by a black bar at $x = 0$. Figure 3.9 shows plots of cross-sections of figure 3.8 at different distances from the aperture, specifically figure 3.9(e) shows the beam intensity profile at a distance of $25\mu m$ away from the aperture which is approximately the experimental distance of the target from the aperture. The full-width half maximum(FWHM) beam size at $0.6THz$ is $112\mu m$ at a distance of $25\mu m$ from the aperture. This calculation is an approximation which

does not take into account the conductivity of the waveguide flange. A finite element analysis for a waveguide radiating into free-space was conducted to account for the conductivity of the flange. An analytical solution for the magnetic field distribution outside a flanged waveguide can be found in [32]. The ratio $\frac{2\pi a}{\lambda}$ in the results presented in [32] is 2, which corresponds to a frequency of approximately 1.9THz for a waveguide plate spacing of $100\mu m$, where a is half the distance of the plate spacing of the parallel plate waveguide. The finite element results were compared to the results in [32]. Figures 3.10 and 3.11 are in terms of normalized distances, $\frac{y}{a}$. Cross-sections at a distance $25\mu m$ from the finite element solution and the analytical solution are shown in figure 3.10(b) and are in good agreement. The normalized electric field amplitude in the y-direction was also evaluated at 0.6THz at cross-section $25\mu m$ away from the waveguide exit plane using the finite element method and is shown in figure 3.11 overlayed with a FDTD simulation and simple diffraction calculation. The FDTD results show that the THz beam is expected to spread to approximately $105\mu m$ while the finite element method shows a spread to $125\mu m$ FWHM at $25\mu m$.

The dependence of the resolution on the waveguide evanescent modes only affects the transmission geometry; in reflection mode, the resolution is still affected by the target-waveguide distance, where the distance determines the waveguide termination characteristics and the coupling efficiency back into the waveguide. The effect of the target-waveguide distance in reflection mode is further discussed in chapter 4.

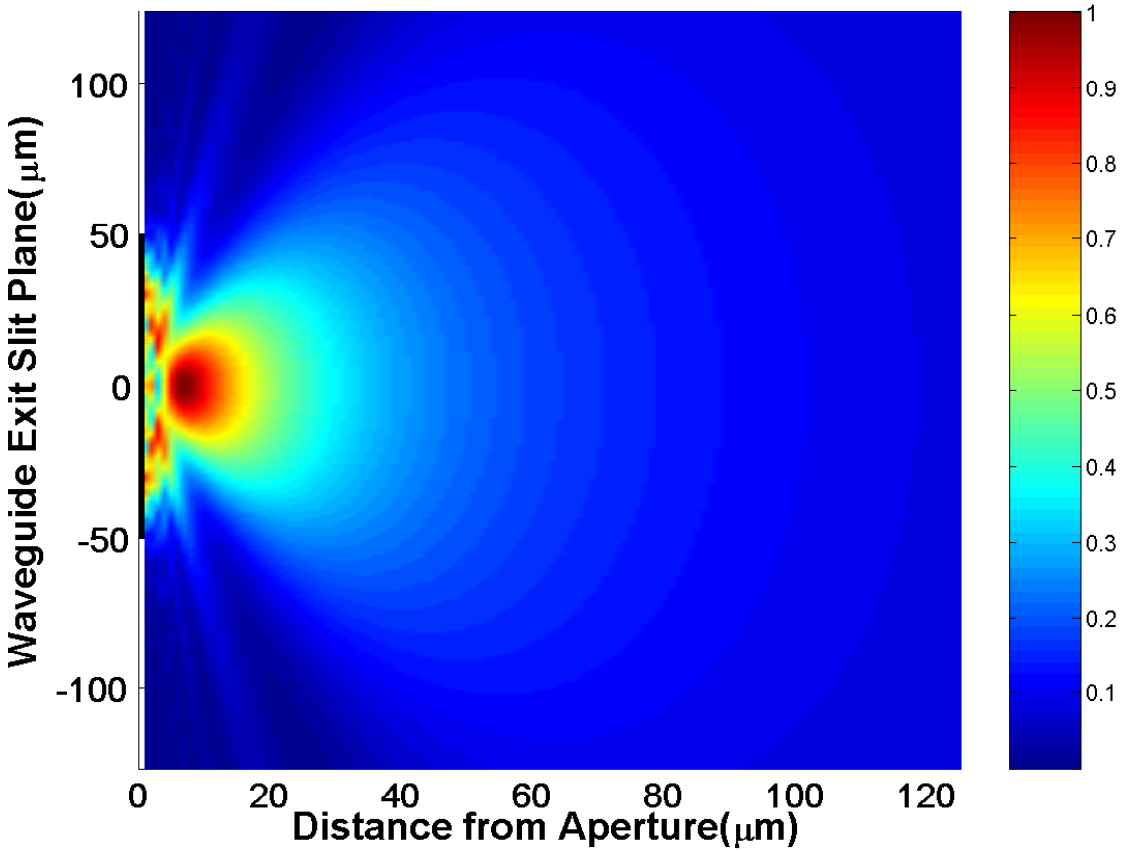

Figure 3.8: Fresnel Diffraction pattern behind $100\mu m$ aperture illuminated at 0.6THz

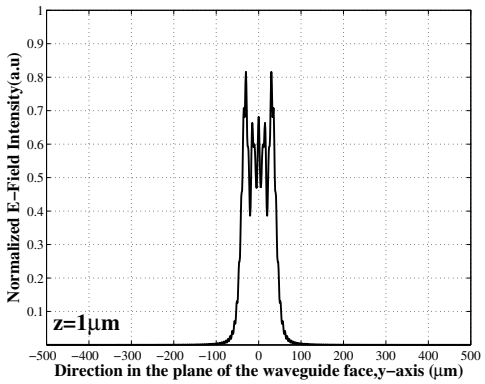

(a) $z = 1\mu m$

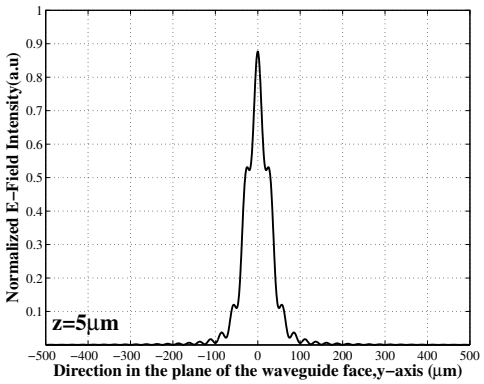

(b) $z = 5\mu m$

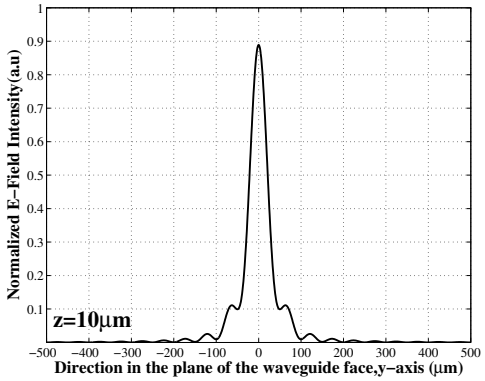

(c) $z = 10\mu m$

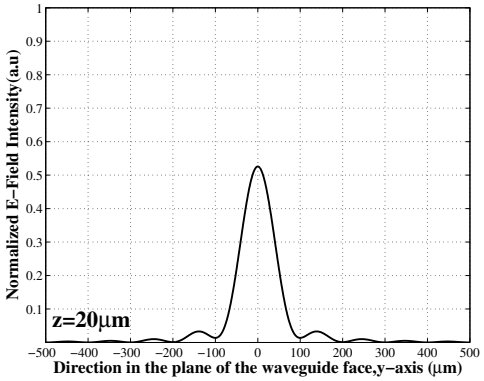

(d) $z = 20\mu m$

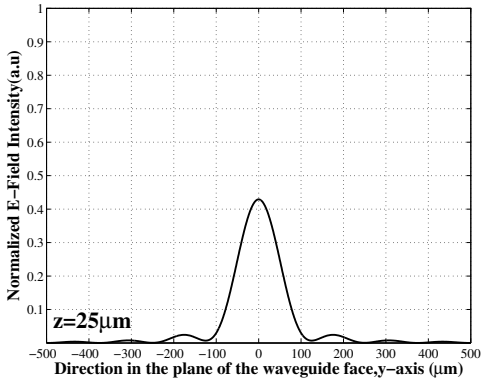

(e) $z = 25\mu m$

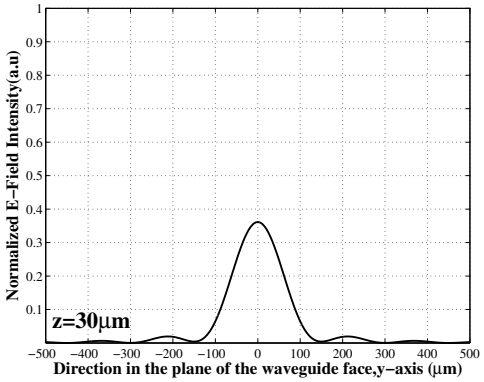

(f) $z = 30\mu m$

Figure 3.9: Fresnel Diffraction pattern from $100\mu m$ aperture

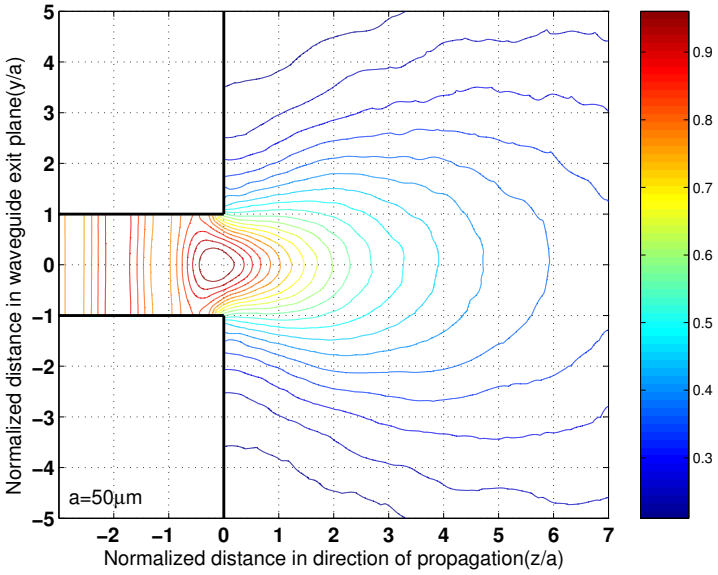

(a) Contour plot of H-field

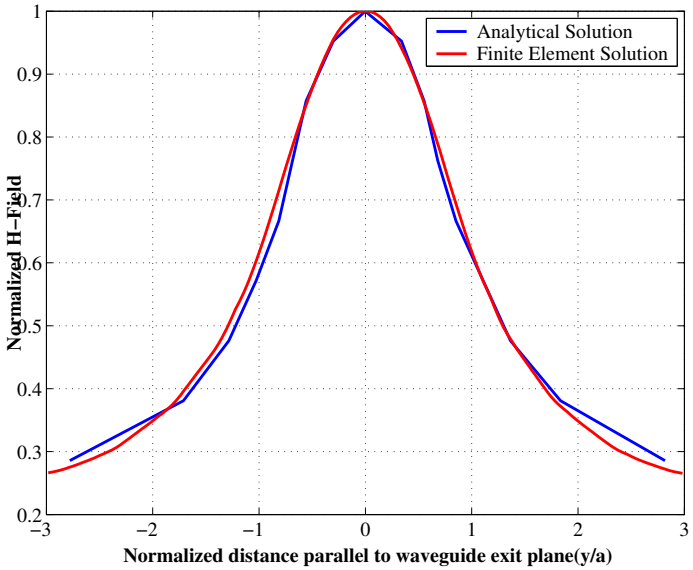

(b) Cross-section at $25\mu m$ away from the aperture

Figure 3.10: Magnetic field distribution

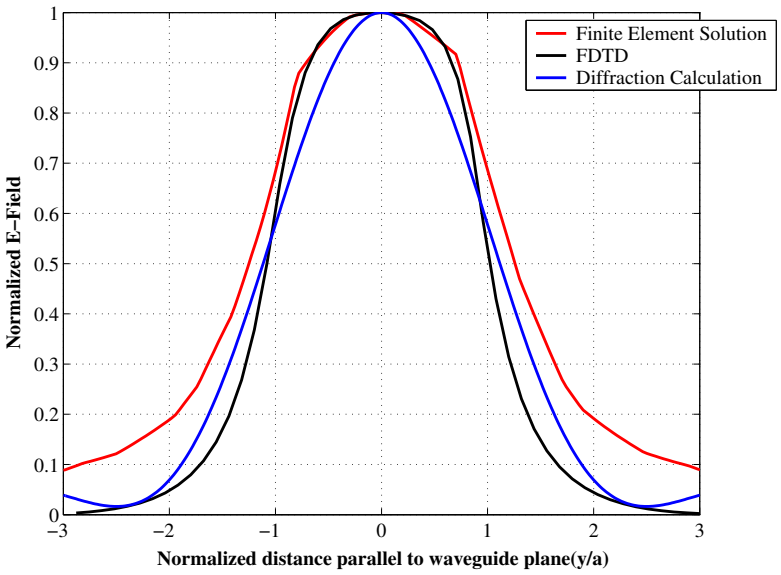

Figure 3.11: Comparision of beam waist simulations

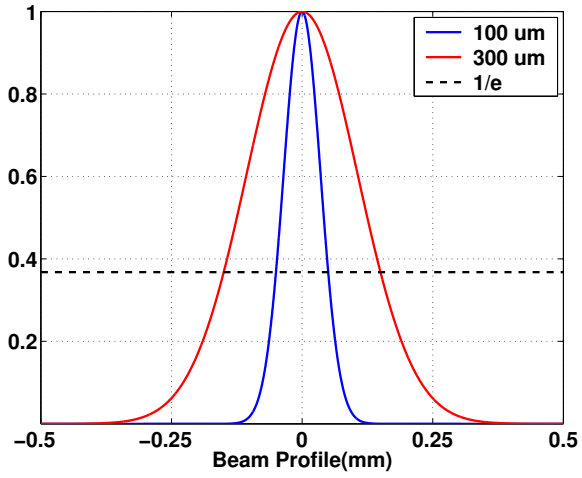

Figure 3.12: Gaussian Beam profile

3.4 Diffraction Limit

The smallest separable distance between two objects to be imaged is generally given as [33]:

$$\Delta l = 1.22\frac{f\lambda}{D} \tag{3.12}$$

where Δl is the distance between the objects or object features, λ is the illuminating wavelength,f is the focal length and D is the diameter of the lens. The relative aperture($\frac{D}{f}$) or f-number of a lens are a measure of the light gathering and resolving power of the optics. Writing 3.12 in terms of f-numbers yields $\Delta l = 1.22\lambda \cdot f\#$. A small f-number will result in better resolution. This is consistent with equation 3.2 for determining the minimum spot size for radiation propagating with a quasi-Gaussian beam profiles where a smaller focal length would result in a smaller beam waist radius. Δl for the cylindrical lenses used in this experiment is $430\mu m$ at 0.6THz.

To illustrate the limit of resolution for the cylindrical lens and the parallel plate waveguide aperture, a Gaussian with a beam waist equal to the illuminating beam of the respective aperture, see figure 3.12, is convolved with the line pattern of an F-Chip shown in 3.13(a). The dimensions for the F-Chip are listed in table 3.1. The cylindrical lens can hardly resolve the separations between the sets of transmission lines and individual lines are not resolved at all, see figure 3.13(b). The parallel plate waveguide aperture on the other hand, should experimentally be able to resolve the transmission line sets numbered 5 and 6 in figure 3.13(a). Line number 4 might be considered just resolved whereas line numbers $1-4$ cannot be individually resolved

F-Chip Line Widths and Gaps	
Transmission Line #	Line Width and Gap Size*
1	5-25-5
2	10-30-10
3	10-50-10
4	10-80-10
5	10-120-10
6	10-200-10

* all dimensions in μm,format: line width-gap-line width

Table 3.1: F-Chip Transmission Line Dimensions

at all, however all sets of transmission lines are clearly separated, see figure 3.13(c). Experimental results for this measurement are presented in chapter 6. The next chapter describes how the apertures discussed in this chapter are used to image the target and how these measurements are interpreted to extract the final image. Also the effect of the THz beam size along the major axis of the aperture is discussed.

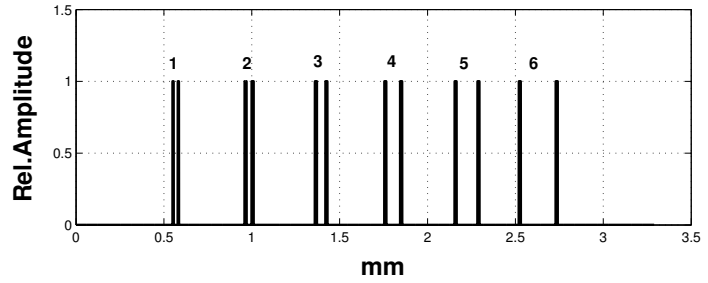

(a) Transmission Line Cross-Section

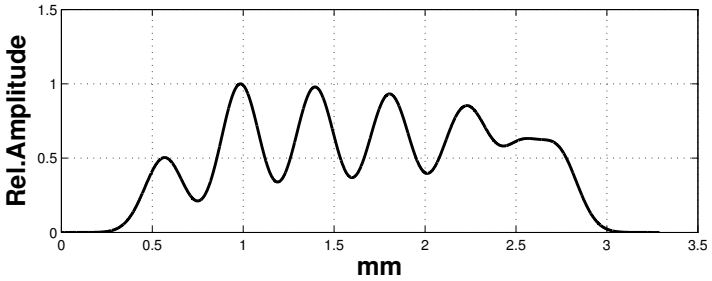

(b) Cylindrical Lens

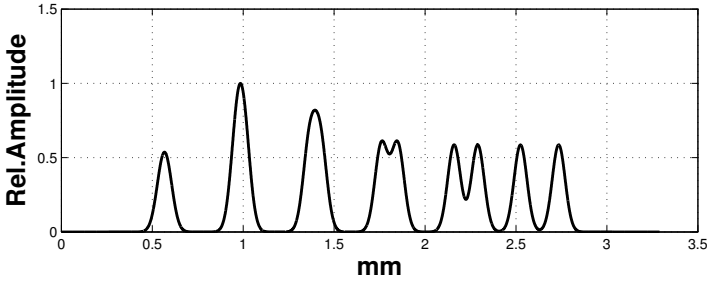

(c) Waveguide Aperture

Figure 3.13: Effect of aperture size on F-Chip measurement

Chapter 4
Background Theory

The previous chapter described the imaging apertures used to image the target as well as the THz beam characteristic of each. This chapter sets the theoretical framework needed to interpret the measurements and extract the image from the measurements produced using each aperture. Also the effect of the frequency dependent beam waist on the final image is discussed. First the radon transform is discussed in terms of its more common usage in the field of computed tomography measurements. Then it is shown that the measurements acquired are also in the form of the radon transform. Further, a modification of the radon transform is presented to account of the frequency dependent beam profile. A radon inversion algorithm,the back-projection operation, is also described. Finally a finite-difference time-domain (FDTD) simulation is performed to measure the coupling efficiency into the waveguide in reflection mode.

4.1 Radon Transform

Unlike raster scan imaging techniques [7], the imaging apertures used in this experiment, whether conventional optics or near-field waveguide apertures, create high aspect ratio illumination of the target. This type of illumination, rather than measuring a single pixel of finite area, measures the profile of the target along the aperture.

A one dimensional measurement of this type is commonly referred to as a *projection*. To image a target using this method, and since the resolution along the length of the aperture is lost, several projections have to be taken at different angles of rotation. These projections are in the form of a radon [34] transform of the target and when sufficient projections are acquired it becomes possible to reconstruct the target using an inversion algorithm. The radon transform has found extensive use in the field of radio astronomy and medical radiology, mainly X-Ray computed tomography scans (CT). Following is a brief description of the radon transform and one of the inversion algorithms, the filtered backprojection algorithm.

Assuming some function $f(x, y)$, the radon transform is defined as the line integral in the xy-plane along path L as shown in figure 4.2 and figure 4.1.

$$I = I_o \exp\left(-\int f(x, y)dl\right) \tag{4.1}$$

$$g(s, \theta) = \ln\left(\frac{I_o}{I}\right) = \int f(x, y)dl \tag{4.2}$$

I_o, I are the incident and measured intensities, respectively and dl is an incremental length along path L. For a given (s_1, θ_1), $g(s_1, \theta_1)$ refers to the line integral along the line orthogonal to the $s - axis$ and intersecting it at s_1. The $s - axis$ is rotated θ_1 degrees off the $x - axis$. This is shown in figure 4.2 however due to the mounting mechanics of the THz optics, the sample will be rotated instead of the optics and the s-axis will always coincide with the y-axis of the experiments. This is in contrast with a CT scanner, where the patient lies stationary and the generation and detection arrays are rotated. Also, figure 4.1(a) shows that the slice to be imaged lies in the same plane as the illuminating beam in CT X-ray imaging. If consecutive slices of a three dimensional object are scanned, then the object can be reconstructed from these two

dimensional slices [35]. This type of measurement and reconstruction is used in CT imaging to obtain a full three dimensional model of a patient. It is important to note that the radon transform is defined as a line integral across some function $f(x, y)$. The fact that the actual measurement is a measurement of absorption is due to the experimental geometry and is not related to the analytical definition of the radon transform.

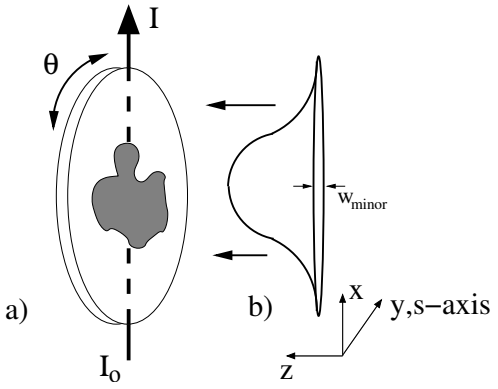

Figure 4.1: Radon transform using (a) pencil type illumination (b) sheet type illumination

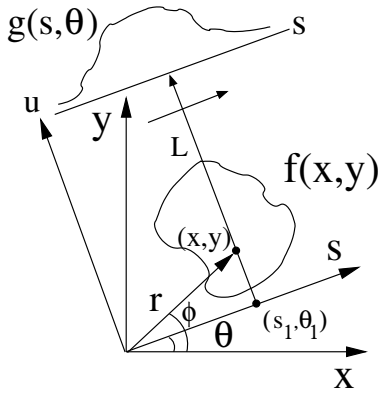

Figure 4.2: Radon Transform

The type of optics used in this experiment differs from the scenario shown in figure 4.1(b) in that the illumination has the spatial extent of a sheet with a Gaussian profile illuminating a line in the plane of the slice and propagating in a direction orthogonal to it. The measurements however can also be interpreted as the radon transform of the target object, and the same reconstruction techniques are used to extract the image. The interpretation of the measured signal and the effect of the Gaussian beam profile on the reconstructed image is further discussed later in this chapter.

This type of imaging method allows for a faster acquisition time compared to pixel-by-pixel imaging and depending on the target complexity of the target the number of

angles can be varied. Therefore, a priori knowledge of the target geometry can be used to reduce the acquisition time even further. Also, using near-field aperture methods, it is possible to generate a sub-wavelength high brightness line source, and utilize image reconstruction techniques to image the target at sub-wavelength resolution.

4.1.1 Definition

Analytically, the Radon transform is defined as [35, 34]:

$$g(s,\theta) = \mathcal{R}\{f(x,y)\} = \int_{-\infty}^{\infty}\int_{-\infty}^{\infty} f(x,y)\delta(x\cdot cos\,\theta + y\cdot sin\,\theta - s,\theta)dxdy \tag{4.3}$$

where $x\cdot cos(\theta) + y\cdot sin(\theta) - s$ is the equation of a line orthogonal to the $s-axis$ and inclined θ degrees off the $x-axis$,i.e. path L in figure 4.2. This is also the equation of the line along the imaging aperture for sheet type illumination shown in figure 4.1(b).

Expressing (x,y) in terms of the rotated coordinate system (s,u) yields:

$$\begin{aligned} s &= x\cdot cos\,\theta + y\cdot sin\,\theta & \qquad u &= -x\cdot sin\,\theta + y\cdot cos\,\theta \\ x &= s\cdot cos\,\theta - u\cdot sin\,\theta & \qquad y &= \ s\cdot sin\,\theta + u\cdot cos\,\theta \end{aligned} \tag{4.4}$$

Equation 4.3 can now be stated in terms of the rotated coordinate system (s,u) as:

$$g(s,\theta) = \int_{-\infty}^{\infty} f(s\cdot cos\,\theta - u\cdot sin\,\theta, s\cdot sin\,\theta + u\cdot cos\,\theta)\,du, \qquad -\infty < s < \infty, 0 \le \theta \le \pi \tag{4.5}$$

du is the incremental length of the path that the integral is evaluated over. Equation 4.5 defining the radon transform, assumes a uniform profile along du, however the THz beam propagates with a quasi-Gaussian beam profile along du, effectively acting as a weighting function for $f(x,y)$ along du. To account for the Gaussian beam profile, equation 4.5 can be modified as follows:

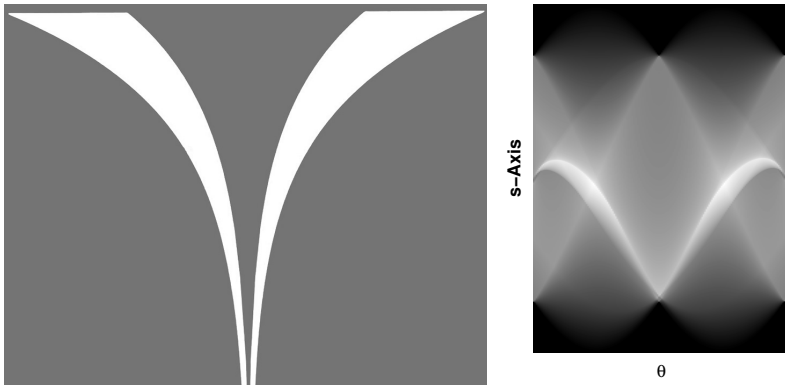

(a) Target Image

(b) Radon Transform of figure 4.3(a)

Figure 4.3: Target Image and its Calculated Radon Transform

$$g(s,\theta,\omega) = \int_{-\infty}^{\infty} f(s\cdot cos\,\theta - u\cdot sin\,\theta, s\cdot sin\,\theta + u\cdot cos\,\theta)\cdot e^{-\left(\frac{u}{w_o(\omega,u)}\right)^2} du,$$
$$-\infty < s < \infty, 0 \leq \theta \leq \pi \quad (4.6)$$

where $w_o(\omega, u)$ is the frequency dependent beam profile illuminating the target along the aperture (u-axis).

The target to be imaged is a planar sub-millimeter horn antenna metalized on a $3in$ silicon wafer; figure 4.3(a) shows an image of the structure. The numerical radon transform of the target is shown in figure 4.3(b). In figure 4.3(b), the horizontal axis corresponds to the angle of rotation $\theta_0 ... \theta_n$ and the vertical axis corresponds to the translation along the s-axis. The computed radon transform of the target shown in figure 4.3(b) does not account for the Gaussian profile.

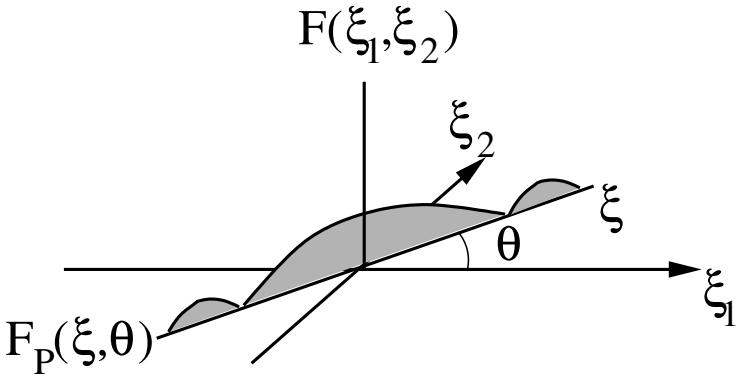

Figure 4.4: Central Slice Theorem

4.2 Radon Inversion Algorithms

The notation used in this section and throughout the remainder of this chapter will use the ξ_n symbol to denote the Fourier transform of a spatial variable. For example $\mathcal{F}\{f(x,y)\} = F(\xi_1, \xi_2)$

There are several different algorithms that can be used to compute the inverse of the radon transform. These inversion algorithms are based on the central slice theorem which relates the one dimensional Fourier transform of the radon transform of a function $f(x,y)$ to the two dimensional Fourier transform of the function. For $f(x,y)$, $g(s,\theta) = \mathcal{R}\{f(x,y)\}$ and

$$G(\xi,\theta) \overset{s}{\underset{\mathcal{F}}{\longleftrightarrow}} g(s,\theta) \tag{4.7}$$

$$G(\xi,\theta) = F_p(\xi,\theta) = F(\xi cos\,\theta, \xi sin\,\theta) \tag{4.8}$$

where F_p is the Fourier transform of $f(x,y)$ in polar coordinates and $F(\xi_1,\xi_2)$ is the two dimensional Fourier transform of $f(x,y)$. The central slice theorem simply states that the one dimensional Fourier transform of the projection set $g(s,\theta)$ with respect to s is equivalent to the slice inclined θ off the ξ_1 axis of the two dimensional

Fourier transform of $f(x, y)$ [35], shown in figure 4.4. The backprojection operation follows directly as a result of the central slice theorem.

4.2.1 Backprojection

Backprojection is defined as [35]:

$$b(x, y) = b_p(r, \phi) = \int_0^{\pi} g(r \cdot cos(\theta - \phi), \theta) d\theta \text{ and } s = r \cdot cos(\theta - \phi) \tag{4.9}$$

where r is the distance from the origin to a point along the line $s = s_1$ in the rotated coordinate system and ϕ is the angle between r and the x-axis, figure 4.2. A backprojected image suffers from blurring due to the backprojection operation resulting in an image that is convolved with the point-spread function of the backprojection operation. This result is independent of the imaging optics used to acquire the projection.

$$f_{reconstructed}(x, y) = f(x, y) \otimes \frac{1}{|r|} \tag{4.10}$$

where $\otimes$ denotes a two dimensional convolution operation, $f(x, y)$ is the original image function and $\frac{1}{|r|}$ is the point-spread function of the backprojection operation.

4.2.2 Filtered Backprojection Algorithm

The algorithm used to reconstruct the images shown in chapter 6 is the filtered backprojection algorithm which uses filtered projections defined as:

$$g_{filtered}(s, \theta) = \mathcal{F}^{-1}\{|\xi| \cdot \mathcal{F}\{g(s, \theta)\}\} \tag{4.11}$$

where $|\xi|$ is the frequency response of a 1-dimensional filter shown in figure 4.5 used to filter the projection data. This term is generally replaced with a filter with a frequency response $H(\xi)$ depending on the type of noise found in the measured projections. The filtered backprojection algorithm is executed as follows:

1. Evaluate the numerical Fourier transform of the projection data with respect to s, $G(\xi, \theta)$
2. Multiply $G(\xi, \theta)$ with the frequency response of the one dimensional filter $|\xi|$
3. Inverse Fourier transform $G(\xi, \theta)$ to obtain $g_{filtered}$
4. Use the backprojection operation to evaluate $f_{reconstructed}(x, y)$

Two common filters are shown in figures 4.5 and 4.2.2. D is a frequency scaling factor which $|\xi| = 0$ for $|f| > D$. The reconstructed images in chapter 6 are filtered using a Hanning filter with different scaling factors.

Figure 4.7 shows the target reconstructed from different number of angles. The filter used was a RAM-LAK filter [35] with $D = 1$. The heavy star pattern is inherent in the backprojection operation and becomes very prominent when reconstructing images from few projection angles. Filtering may help reduce this artifact however more aggressive filtering will reduce the resolution of the image. Another factor in determining the final image quality is the selection of angles to image from. Different sets of of angles, even though having the same number, produce images of different qualities. The images produced in chapter 6 were filtered using a Hanning filter shown in figure 4.2.2.

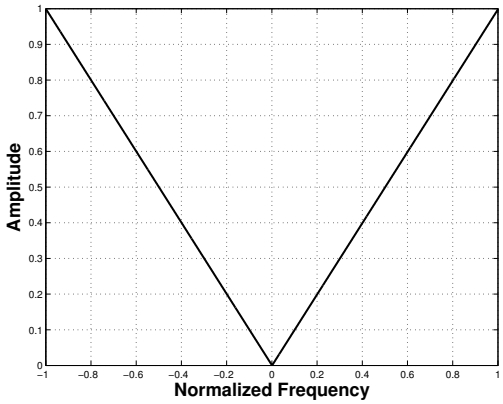

(a) D=1.00

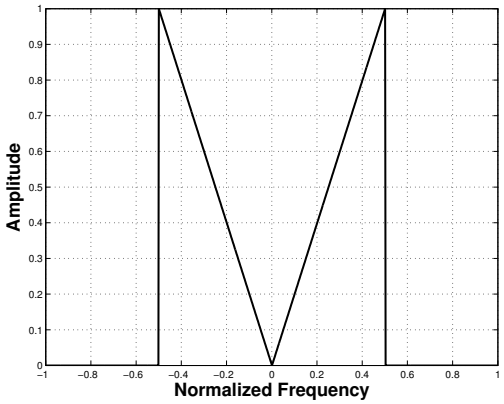

(b) D=0.50

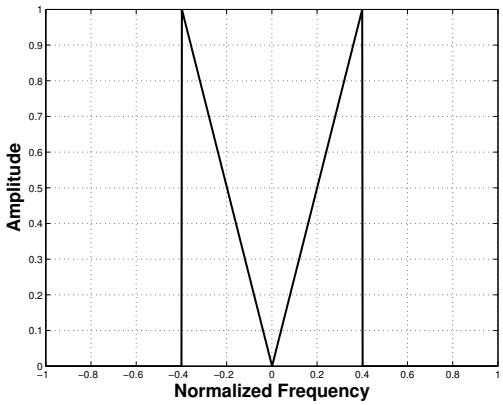

(c) D=0.40

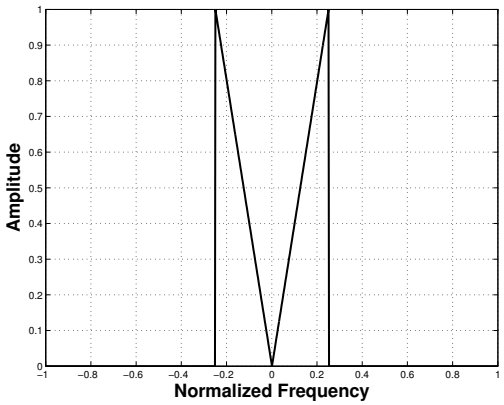

(d) D=0.25

Figure 4.5: RAM-LAK Filter

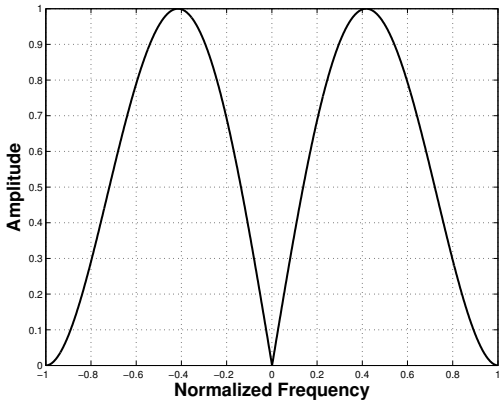

(a) D=1.00

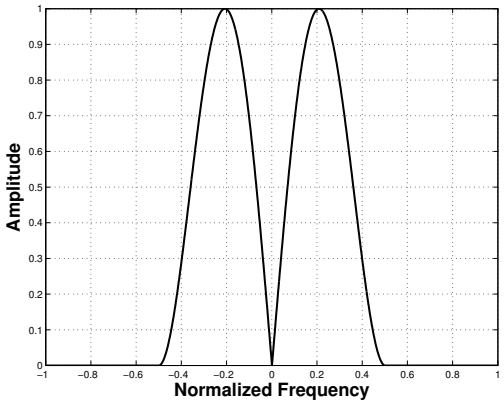

(b) D=0.50

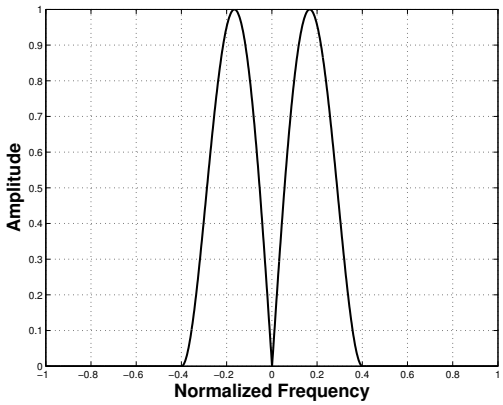

(c) D=0.40

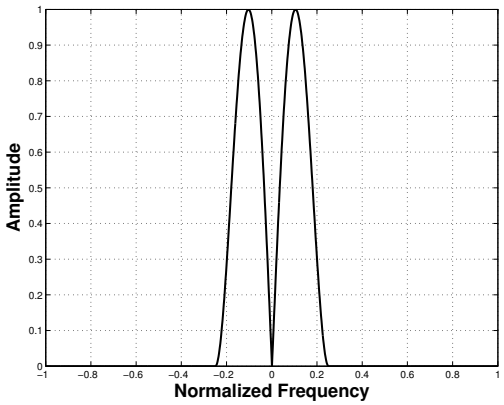

(d) D=0.25

Figure 4.6: Hanning Filter

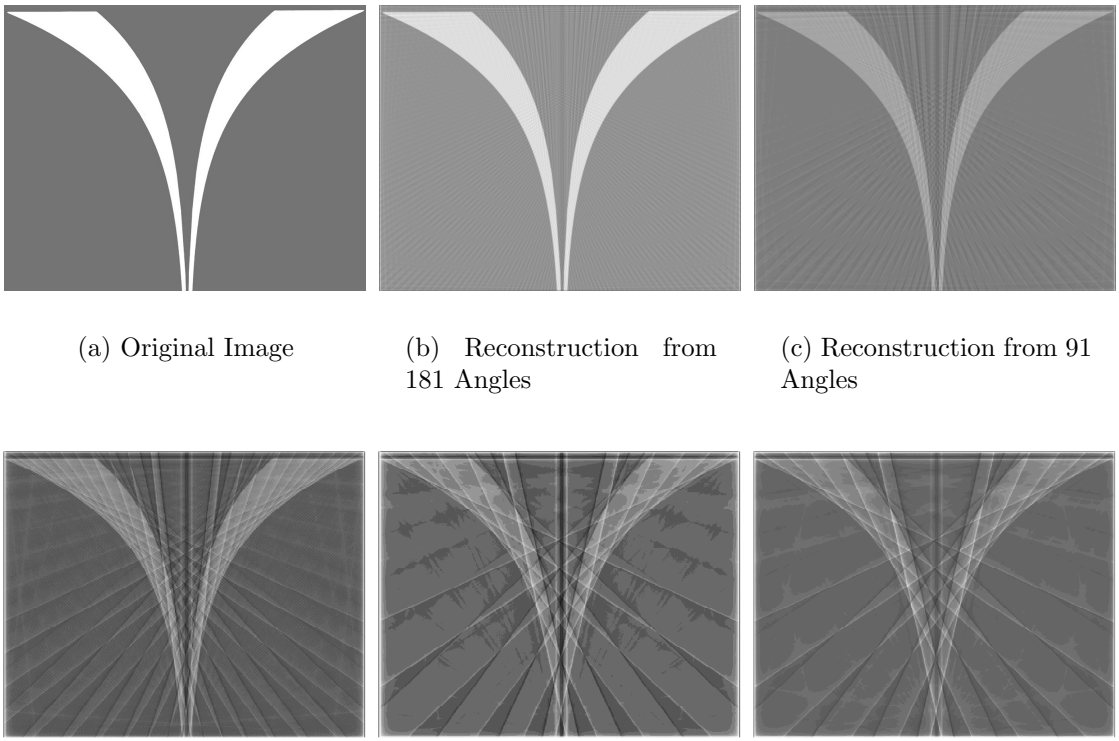

(a) Original Image

(b) Reconstruction from 181 Angles

(c) Reconstruction from 91 Angles

(d) Reconstruction from 37 Angles

(e) Reconstruction from 19 Angles

(f) Reconstruction from 18 Angles

Figure 4.7: Target Image reconstructed from 4.3(b)

4.3 Effect of Gaussian Beam Profile on Reconstruction

Chapter 3 described the cylindrical lens and waveguide aperture and the characteristics of the THz beam created. The effect of the THz beam profile along the u-axis on the radon transform was shown previously, however its effect on the reconstructed image was not discussed.

Taking the Fourier transform of $g(s,\theta)$ along s yields:

$$G(\xi,\theta) = \int_{-\infty}^{\infty} g(s,\theta) e^{-\jmath 2\pi\xi s} ds \tag{4.12}$$

and substituting equation 4.6 that accounts for the Gaussian beam profile for the projection set into 4.12 gives:

$$G(\xi,\theta) = \iint_{-\infty}^{\infty} f(s\cdot cos\,\theta - u\cdot sin\,\theta, s\cdot sin\,\theta + u\cdot cos\,\theta)\cdot e^{-\left(\frac{u}{w_o(\omega,u)}\right)^2} e^{-\jmath 2\pi\xi s}\, ds\, du \tag{4.13}$$

using equations 4.4 to convert to Cartesian coordinates:

$$G(\xi,\theta) = \iint_{-\infty}^{\infty} \overbrace{f(x,y)\cdot e^{-\left(\frac{-x\cdot sin\,\theta + y\cdot cos\,\theta}{w_o(\omega,-x\cdot sin\,\theta+y\cdot cos\,\theta)}\right)^2}}^{f'(x,y)} \cdot e^{-\jmath 2\pi(x\xi cos\,\theta + y\xi sin\,\theta)}\, dx\, dy \tag{4.14}$$

The effect of the Gaussian beam profile along the major axis of the aperture is in the form of an effective image density function, $f'(x,y)$, equal to the original image density function and weighted by the Gaussian profile as in equation 4.14. Since there is a θ dependence in 4.14 for $f'(x,y)$, θ has to be accounted for when calculating $f'(x,y)$ as follows:

$$f'(x,y) = \sum_{\theta=0}^{\pi} f(x,y)\cdot e^{-\left(\frac{-x\cdot sin\,\theta + y\cdot cos\,\theta}{w_o(\omega,-x\cdot sin\,\theta+y\cdot cos\,\theta)}\right)^2} \tag{4.15}$$

where θ varies according to the step size of rotation, for the data acquired experimentally 10^o per iteration. When $f'(x, y)$ is evaluated from projection, the summation in equation 4.15 is inherently accounted for in the backprojection operation.

The minimum spot size of the THz beam along the minor axis of either aperture and the Gaussian profile along the major axis of the aperture affect the final reconstructed image. The effect of the resolution limit was shown in equation 3.1, which depends on the diffraction limit of the cylindrical optics and the plate spacing of the waveguide aperture. The effect of the filtering and interpolation performed in the backprojection operation is not accounted for in the above treatment, but also has an effect on the image resolution, however not in the optical sense. The size of the THz beam along the major axis determines the size of the object that the system can image at a given frequency, where this quantity ultimately determines the signal to noise ratio of the imaging system. The frequency dependence of the THz beam waist at the imaging plane results in that reconstructions at higher frequencies, and due to their smaller beam waist diameter, do not provide sufficient coverage across the target, resulting in a lower signal to noise ratio. Figure 4.8(a) shows the calculated resolution of the confocal lens system. The effect of the Gaussian beam profile along major axis of the aperture is shown in figure 4.8(b) and can be seen to be practically negligible, however for smaller beam diameters the effect becomes prominent. Figures 4.8(c) and 4.8(d) show the reconstructed image using a cylindrical lens in a reflection geometry. The following sections apply the above concepts to the measurements acquired in both geometries.

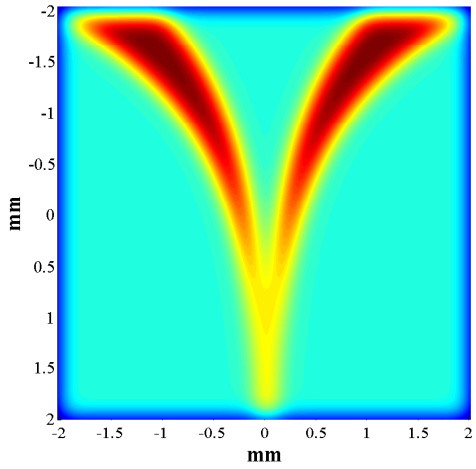

(a) Trumpet convolved with $300\mu m$ Gaussian

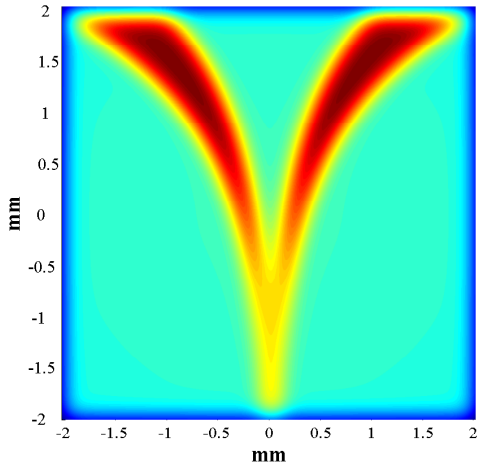

(b) Effect of Gaussian along major axis according to equation 4.15

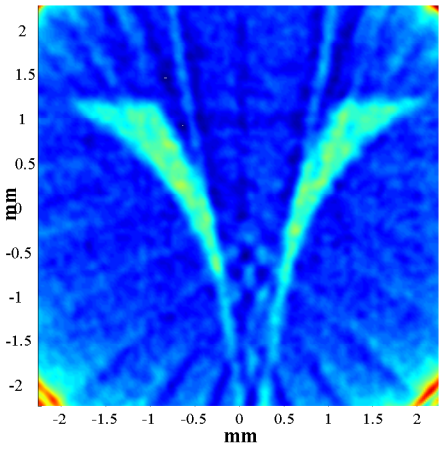

(c) Target reconstructed using cylindrical lens in reflection geometry

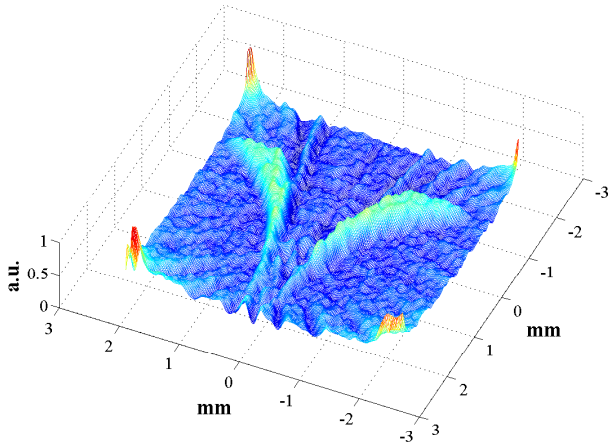

(d) 3D view of figure 4.8(c)

Figure 4.8: Effect of Gaussian beam profile along major axis of aperture

4.4 Transmission Geometry

In transmission mode, the measured signal can be interpreted as follows:

$$g(s,\theta) = \int_{-\infty}^{\infty} I(l,\omega) \cdot f(l) \cdot e^{-\alpha(l)\Delta z} dl \tag{4.16}$$

l and dl are the length and incremental length along the imaging aperture(x-axis in figures 5.3 and 5.1, respectively. $I(l,\omega)$ is the frequency dependent beam profile along l. $f(l)$ is the image density function along l. $\alpha(l)$ is the absorption in the direction of propagation z for a given l and Δz is the sample thickness. Due to the shallow skin depth of aluminum at terahertz frequencies, the exponential term in equation 4.16 is either 0 or 1.

4.5 Reflection Geometry

In reflection geometry, the reflection off the surface of the target is measured. This means that the measured THz signal is dependent on reflectivity of the material it is incident on. In the case of metals, the reflection is nearly 100% and the measure THz signal can be written as:

$$g(s,\theta) = \int_{-\infty}^{\infty} I(l,\omega) \cdot \Gamma(l,\omega) dl \tag{4.17}$$

where $\Gamma(l,\omega)$ is the frequency dependent reflection coefficient at some incremental length along the aperture, and $I(l,\omega)$ is the frequency dependent beam profile also along l. The image can be reconstructed from the integral reflectivity measurement in equation 4.17.

For the cylindrical lens aperture, the target is placed at the focus of the lens, and the projections are collected as described previously.

4.5.1 Reflection Mode - Waveguide Aperture

The target to be imaged, when placed at the output side of the waveguide, effectively acts like a termination, and determines the reflection coefficient. The magnitude of the reflection coefficient was evaluated numerically to determine the effect of the waveguide-target distance on the measured signal. The Finite Difference-Time Domain(FDTD) [36, 37] method was used to determine the reflection coefficient with a Perfect Electrical Conductor(PEC) terminating the waveguide at different locations parallel to the waveguide exit plane. A similar experiment was conducted in [38] at a single frequency for distances from direct contact to several wavelengths away from the waveguide. The experimental results obtained were compared to two numerical models. The model of interest here, and with easy applicability in the time domain, is the wedge diffraction model [38], where the effective reflection coefficient is expressed as [38]:

$$\Gamma = \Gamma_s + \Gamma_p = \Gamma_s + \sum_{n=1}^{\infty} \Gamma_n \tag{4.18}$$

where Γ_s is the free space reflection coefficient and Γ_p is the reflection coefficient due to the metal sheet. The latter reflection coefficient is expressed as a sum of individual reflections that result from the spacing between the metal sheet and the waveguide coupling back into the waveguide.

The FDTD code used to perform the simulation is an adaptation of a FDTD code that has been previously used and verified for other work. The excitation source used in the FDTD simulation and its corresponding spectrum are shown in figure 4.9. The waveguide walls were modeled as PECs. The computational grid consists of 200 points in the y-direction and 800 points along the direction of propagation, the

z-axis. The grid resolution was set at $\frac{\lambda}{100} = 6\mu m$ where $\lambda = 600\mu m$ corresponding to 0.5THz. The time-step was 0.01ps. The results of the FDTD simulation are shown in figure 4.10. Figure 4.10(a) shows the magnitude of the reflection coefficient when the metal plate is in direct contact with the waveguide aperture. As the distance between the metal sheet and the waveguide aperture increases, the coupling efficiency of the low-frequency components decreases. Figures 4.10(b) and 4.10(c) show the magnitude of the reflection coefficient for $12\mu m$ and $18\mu m$ separation. As the distance is increased even more, the high diffraction of low frequencies results in lower coupling back into the waveguide. This decrease in coupling efficiency at larger separations is shown in figure 4.10(d). Figure 4.11 shows a top view of the THz pulse propagating in the z-direction. For small distances separating the metal sheet and the waveguide exit plane, the summation term in equation 4.18 is mainly determined by the first term, Γ_{p1}, since there is no reflection from the waveguide-air interface. The only reflection is due to the metal sheet as seen in figure 4.11(a). As the distance between the PEC sheet and the waveguide exit plane is increased, reflections off the PEC sheet partially couple back into the waveguide and partially reflect of it and bounce back and forth between the waveguide and the metal sheet. This is shown in figure 4.11(b) where the gap between the waveguide exit plane and the metal sheet is approximately $300\mu m$. The FDTD results at small separations agree well with results published in [38]. This chapter discussed the radon transform and the backprojection algorithm to interpret the data and extract images from that data. Also the physical meaning of the measurements for both geometries was discussed. The next chapter describes the imaging configurations for both geometries and the modes of data acquisition.

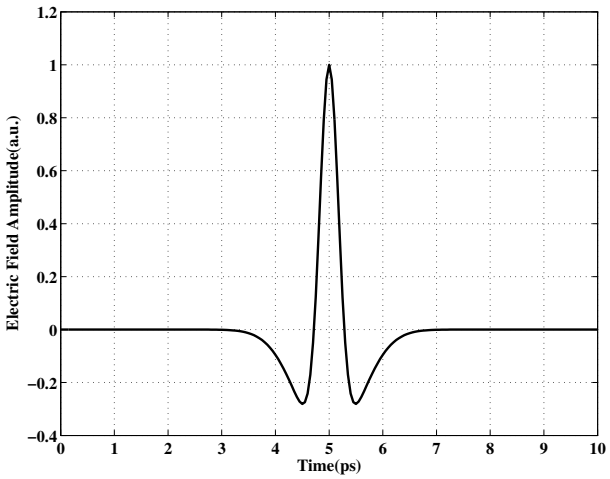

(a) THz pulse used in FDTD calculation

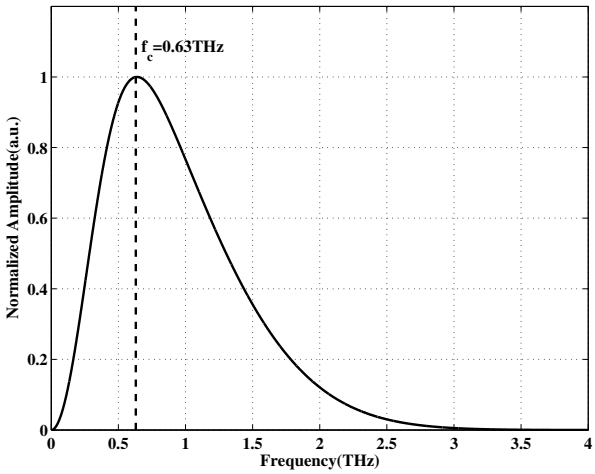

(b) Frequency spectrum of 4.9(a)

Figure 4.9: THz pulse shape used in FDTD simulation and its corresponding frequency spectrum

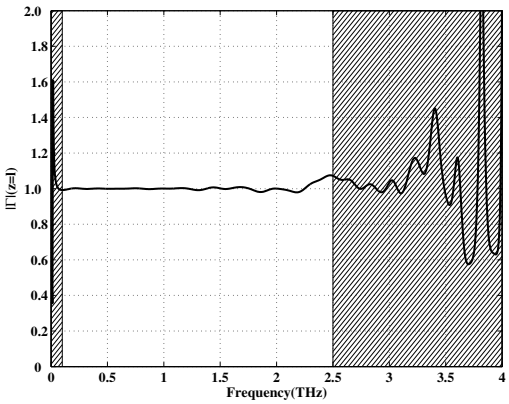

(a) Gap=$0\mu m$

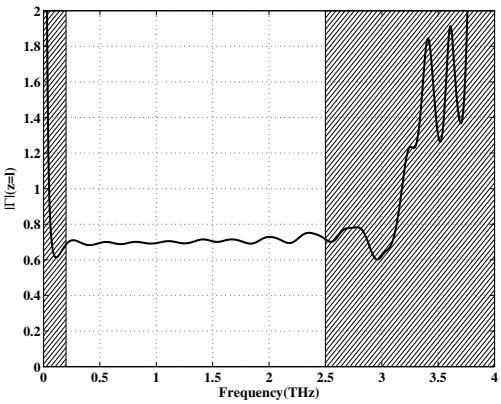

(b) Gap≈ $12\mu m$

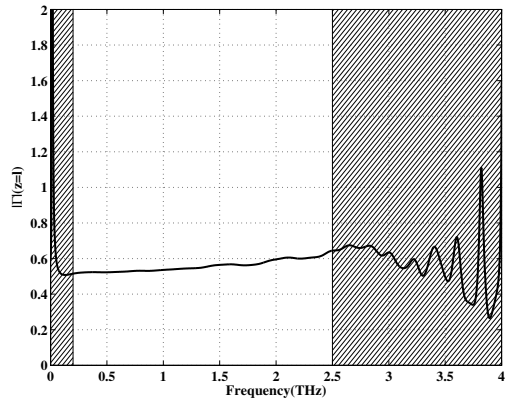

(c) Gap≈ $18\mu m$

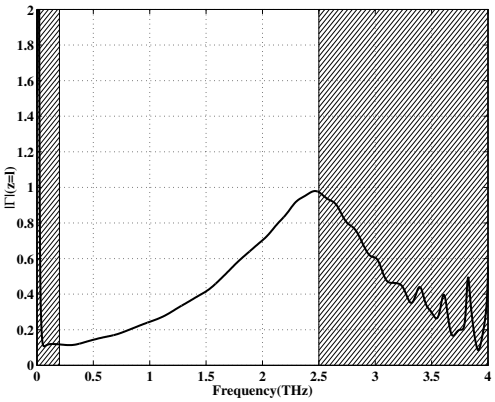

(d) Gap≈ $60\mu m$

Figure 4.10: Magnitude of reflection coefficient $\Gamma(\omega)$ - FDTD

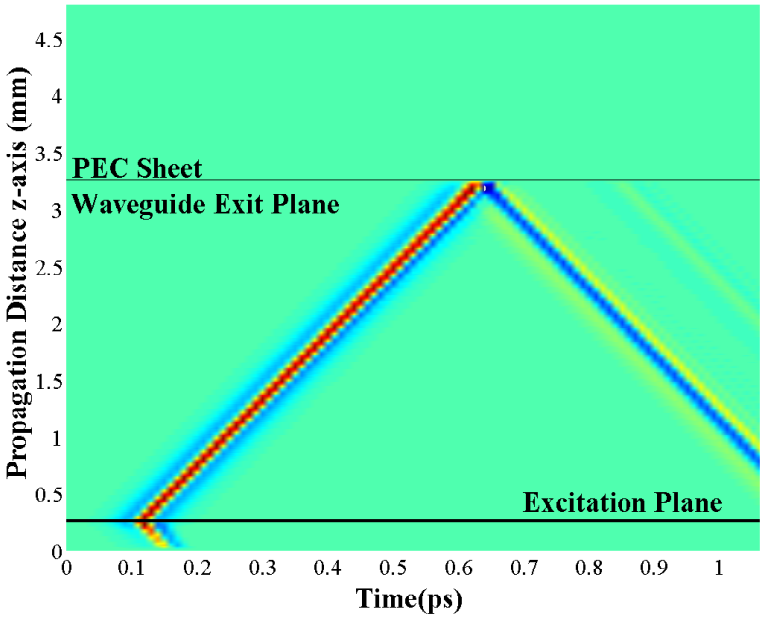

(a) PEC-Waveguide distance≈ $18\mu m$

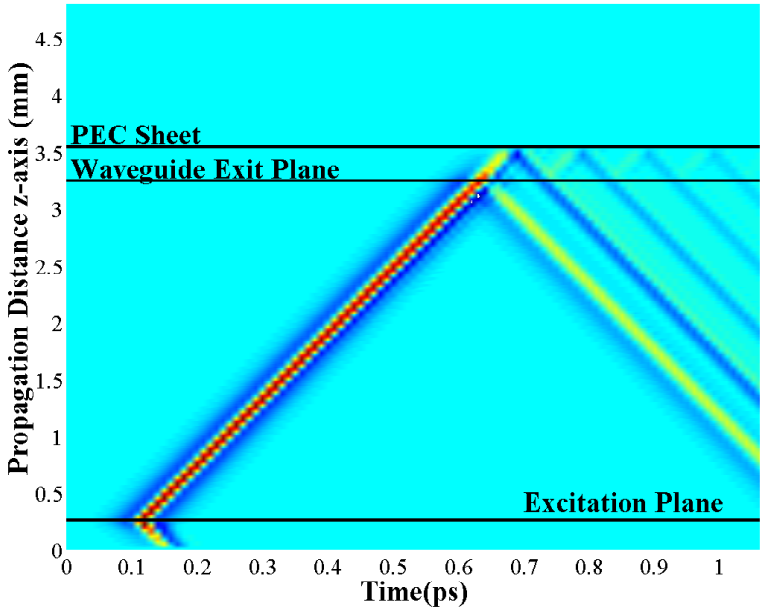

(b) PEC-Waveguide distance≈ $300\mu m$

Figure 4.11: FDTD simulation of THz pulse reflection off a metal sheet

Chapter 5
Imaging Setup

As described in chapter 4, the radon transform requires sample movement along the rotated s-axis, as illustrated in figure 4.2. This is accomplished by mounting the target on a rotation stage that is in turn mounted on a translation stage. The translation movement is orthogonal to the optical axis. The sample translation stage is motorized, however the rotation stage is manual. For both imaging geometries, the data acquisition methods and the sample translation mechanics are the same, except for the large clear aperture rotation stage is replaced with a smaller rotation stage in reflection mode, where the clear aperture is not needed.

The following sections describe in more detail the individual imaging setup for transmission and reflection imaging and the the methods of data acquisition. The coordinate convention used is shown in figure 5.1 for transmission and figure 5.3 for reflection mode. For all imaging configurations, it is essential that the translation of the sample holder stage is orthogonal to the optical axis. Experimentally this has been verified using a dial micrometer.

5.1 Data Acquisition

The image data was acquired using two different methods described below. The difference lies mainly in the signal to noise ratio and the amount of data collected, where using a lock-in amplifier resulted in fairly small data files of size less than

$100Kbyte$. Using a rapid scanning delay line, the data files were significantly larger, reaching a size of approximately $40Mbyte$.

5.1.1 Using a Lock-in Amplifier with no time resolved data

A lock-in amplifier requires the use of a mechanical chopper to modulate the transmitted THz beam. The chopper also provides a reference signal for the lock-in amplifier, and only a signal at the same frequency as the reference frequency is amplified. Lock-in detection allows for very high signal-to-noise ratios in excess of 10,000:1. Figure 2.3 shows a THz pulse and its corresponding frequency spectrum. Typically, a full time scan is acquired using a computer controlled optical delay line. A single data point is collected and the delay line advanced, however it is not feasible to acquire full time scans for a complete image considering the time it takes to complete a full scan. Therefore, for all image data that was collected using a lock-in amplifier, only the peak of the signal was acquired. Practically this means, that the optical delay line was adjusted to coincide with the peak of the THz pulse, and changes only due to the sample movement were acquired. This of course assumes that the sample does not incur any changes in timing. This method does not retain any spectral information from the data scans.

5.1.2 Rapid Scanning Delay Line

Full time waveform scans using a rapid scanning delay line(All except reflection mode waveguide aperture). A retroreflector mounted on a speaker provided an approximately 80ps relative delay. The speaker was driven by a $17Hz$ sine wave, which also

supplied the trigger for the data acquisition computer. The photocurrent is converted into a voltage using a high-speed low noise current amplifier. An active bandpass filter is also used for further signal amplification and filtering. This type of delay line allows for much faster data acquisition, at the cost of lower signal to noise ratio. The output of the bandpass filter is then fed into a data acquisition computer. Several scans are acquired and averaged to improve the SNR.

Since time resolved scans are acquired, the image data can be extracted in two ways.

1. Compiling the image data from the peak of the measured signal for each time resolved scan.

2. Performing a Fourier transform of the time resolved scans and compiling the image data from discrete frequencies.

The data can now be converted into an image using the methods in chapter 4.

5.2 Transmission Geometry

The general configuration of the transmission mode imaging setup is similar to a standard THz-TDS setup, with the imaging optics inserted at the beam waist w_2, see figure 5.2. Both cylindrical lenses are mounted inside precision rotation stages which are mounted on tip-tilt and xyz-translation stages. The receiver side cylindrical lens is also mounted on a second rotation stage to allow rotation in the yz-plane, see figure 5.1. The entire receiver side cylindrical lens mounting mechanics is mounted on a kinematic base allowing for easy removal and replacement. Because the target

is mounted on a large rotational mount it is necessary to remove the cylindrical lens on the receiver side completely to insert the target. This is also the case using the waveguide aperture. This setup allows for extreme flexibility when aligning the optics. The imaging target is mounted on the rotation/translation stage described earlier and carefully positioned at the imaging plane and the cylindrical lens mechanics is re-inserted.

5.2.1 Confocal Cylindrical Lens Setup

Focusing the THz beam using a cylindrical lens creates a high aspect ratio elliptical focus with a frequency independent beam profile along the minor axis of the elliptical spot as described in chapter 3. The beam profile along the major axis of the focal spot will remain frequency dependent but is assumed to be uniform for the spatial extent of the target to be imaged. This practically limits the dimension of the target size. The target is placed at the focal plane, which is also the image plane for this configuration. The rotation stage that holds the target has to be aligned such that its center coincides with the optical axis of the system. This is accomplished by taking more projections on both side of the optical axis along the $s - axis$ than needed and numerically centering the data.

Now, an image can be acquired by either lock-in detection or using a rapid scanning delay line to obtain time resolved data for each projection,see figure 5.1.

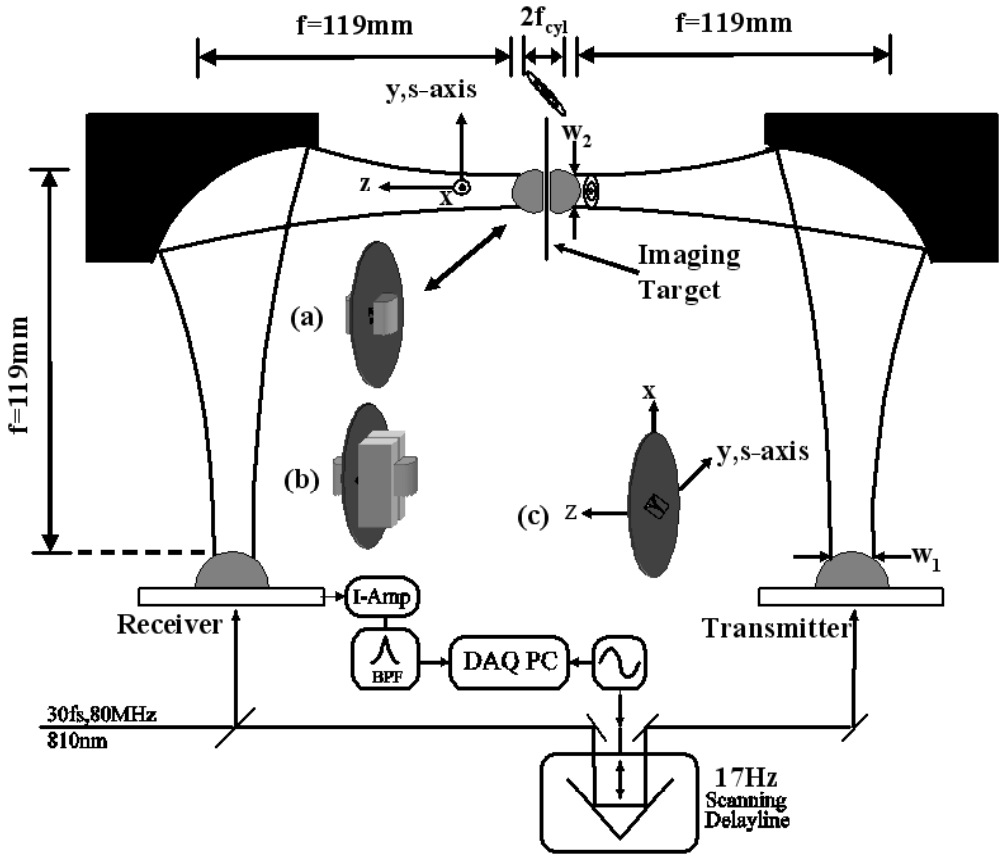

Figure 5.1: Transmission Imaging Configuration with Rapid Scanning Delay Line

5.2.2 Waveguide Setup

The waveguide imaging configuration is very similar to the confocal cylindrical lens setup described in the previous section. The two lenses are moved apart from their confocal position and the parallel plate waveguide is inserted in between. After the waveguide and cylindrical lenses are aligned, the lens coupling out of the waveguide is removed and the sample placed in near contact($\approx 25\mu m$) with the waveguide exit slit, which serves as the imaging aperture, see figure 5.2. Finally the cylindrical lens is placed back and in contact with the backside of the sample. An image is acquired in the same fashion as before.

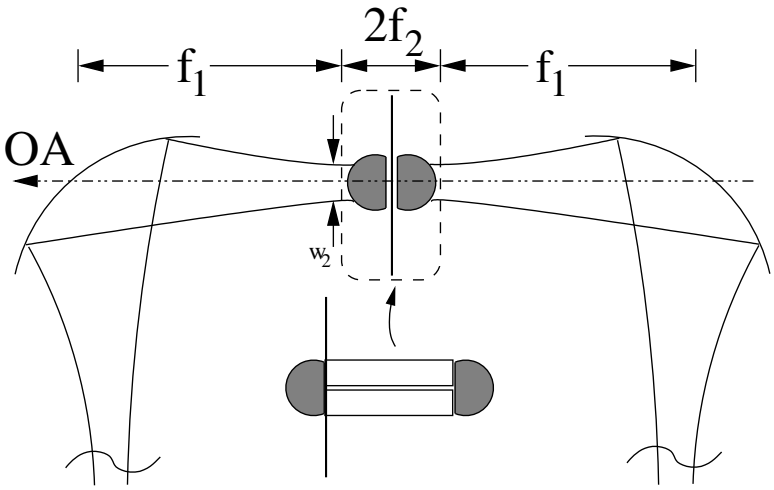

Figure 5.2: Imaging optics inserted at beam waist

5.3 Reflection Geometry

Reflection imaging is performed using the configuration shown in figure 5.3. The collimated THz beam is partially reflected at the beam-splitter. A frequency dependent beam waist is created at w_2. The same cylindrical lens used in the transmission mode configuration is placed at w_2. This again creates a high aspect ratio beam waist and the focus used to image the target. Also the waveguide aperture can be placed behind the cylindrical lens. This creates an easily changeable system that can utilize either the cylindrical lens or the waveguide as an imaging aperture. The reflected signal from the target passes through the beam-splitter and onto the receiver. An inherent limitation to the signal to noise ratio in the reflection mode configuration lies in the fact that the beam-splitter reduces the detected THz radiation to a quarter of the signal compared to the transmission mode configuration. The same mechanical mounting is used for this configuration, where the translation along the s,y-axis is shown in figure 5.3.

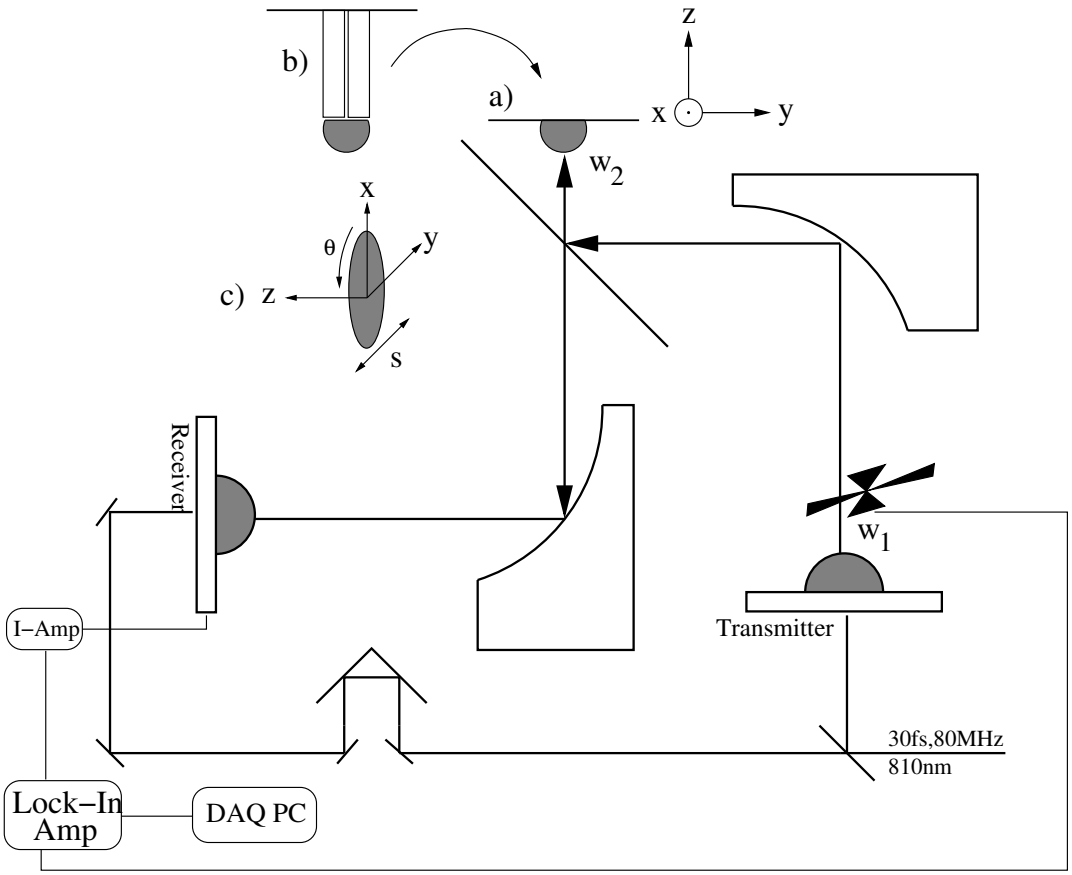

Figure 5.3: Reflection Imaging Configuration with lock-in detection

Chapter 6
Results

The results are presented into two sections, one for each imaging configuration. The data acquired using the non-time resolved lock-in method is first plotted in radon space,i.e. θ vs. s, then this data is used to reconstruct the final image. The time-resolved data is processed in two ways and also plotted in radon space:

1. Sampling the signal maximum or minimum of the temporal waveform

2. By performing a Fourier transform for each projection and sampling discrete frequencies for reconstruction

The data in radon space is then used to reconstruct the individual images. The reconstruction is performed using the filtered backprojection algorithm described in chapter three. To filter out the high frequency noise, one dimensional Hanning window with a scaling factor of $D = 0.25$, $D = 0.4$ and $D = 0.5$ was used. As can be seen from the reconstructed images in figures 6.2 and 6.3, there is a trade-off between the final image resolution and filtering. The image quality could be further improved by using other image enhancement techniques, however for the purpose of comparing the individual results, this was not pursued.

6.1 Data

6.1.1 Transmission Mode

Lock-In

The data collected using lock-in detection does not have any time information;the delay line is adjusted for maximum signal and the data is acquired as described earlier. This type of data acquisition makes the data very susceptible to any movement of the target along the direction of propagation. Any such movement will incur a change in timing in addition to loss of resolution due to movement away from the beam focus. Figure 6.1 shows the acquired data for both the cylindrical lens and waveguide aperture. The projections from the first angle,$g(s, \theta = 0)$ are shown in figure 6.1. In addition to the improvement in contrast, there is a clear increase in the signal-to-noise ratio using the waveguide aperture. Consequently, when performing the filtered backprojection operation to extract the image, the cylindrical lens data will require more filtering to remove the spatial high-frequency background noise. This filtering will also affect the effective resolution of the final image whereas the waveguide aperture will require less filtering to achieve the same degree of attenuation of background noise. Reconstructed images for the parallel plate waveguide and cylindrical lens aperture are shown in figures 6.2 and 6.3 respectively. The reconstructed waveguide aperture image with $D = 0.5$, shown in figure 6.3(c), exhibits visibly less background noise compared to the cylindrical lens image 6.2(c).

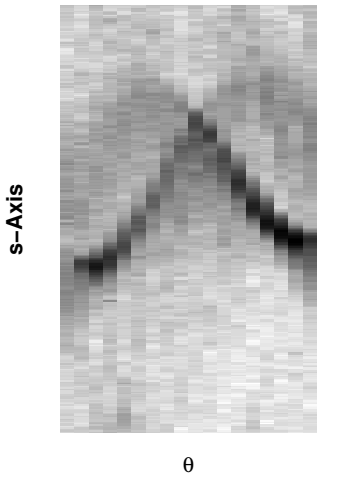

(a) Cylindrical lens

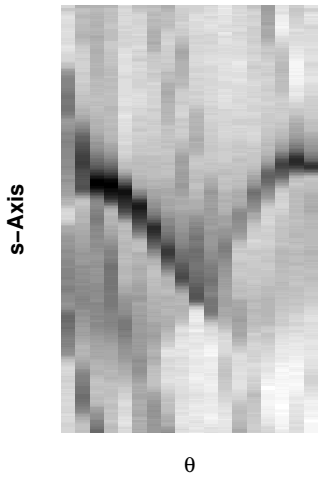

(b) Waveguide aperture

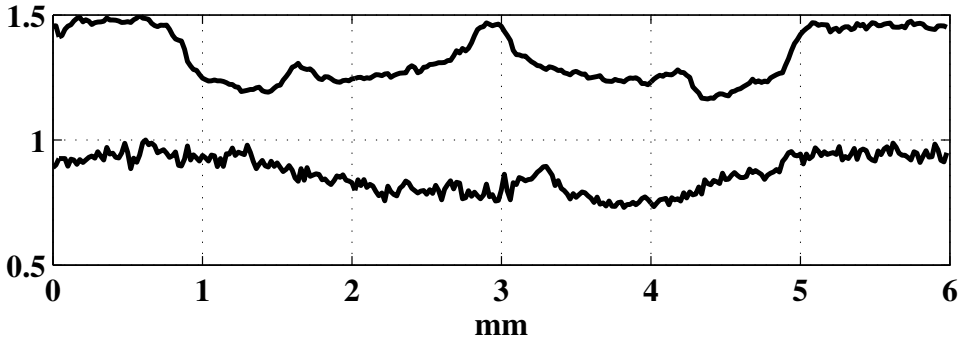

(c) First Projection Angle for waveguide aperture (top) and cylindrical lens (bottom)

Figure 6.1: Raw data in radon space

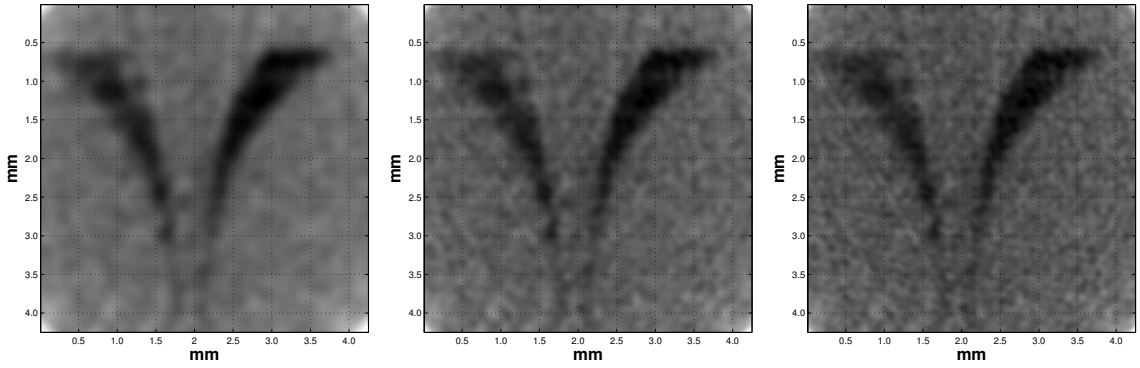

(a) D=0.25 (b) D=0.4 (c) D=0.5

Figure 6.2: Cylindrical lens reconstruction - Lock-in

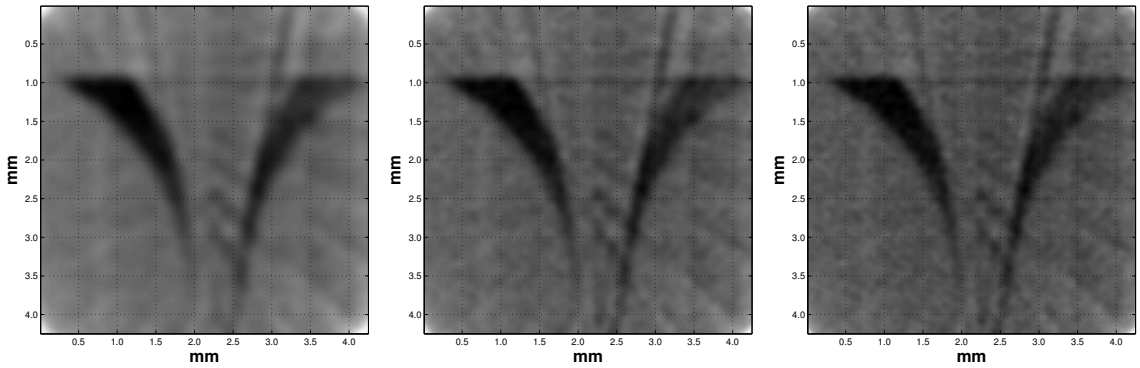

(a) D=0.25 (b) D=0.4 (c) D=0.5

Figure 6.3: Waveguide aperture reconstruction - Lock-in

Rapid Scanning Delay Line

Figure 6.4 shows the acquired time resolved scans for all angles stacked back to back. There is a time shift in the first few projections that are acquired which can be traced back to the mounting mechanics. Practically, this time shift is accounted for insofar that the peak of the signal is sampled regardless of where in time the peak occurs, however the resulting loss in resolution due to the movement of the sample away from the imaging plane cannot be compensated. Figures 6.13(a) and 6.13(b) show the time resolved scans for the first projection angle for the cylindrical lens and waveguide aperture, respectively.

Figures 6.6(a) and 6.6(b) show the first projection angle of the data compiled from the peaks in figure 6.4. The increase in resolution using the waveguide aperture is evident from figure 6.6(b), also there is a clear increase in the signal-to-noise ratio when compared to the cylindrical lenses. Figure 6.5 shows the image reconstructed from the peaks similar to the projections shown in figure 6.6.

Figures 6.7 and 6.8 show the first projection angle $\theta = 0^o$ for both apertures at different frequencies. As can be seen from these figures, projections at high frequencies suffer from an increase in noise. The reconstructed images from discrete frequencies are shown in figures 6.10 and 6.12 for the cylindrical lens and waveguide apertures, respectively. Figures 6.9 and 6.11 show the respective filtered data in radon space.

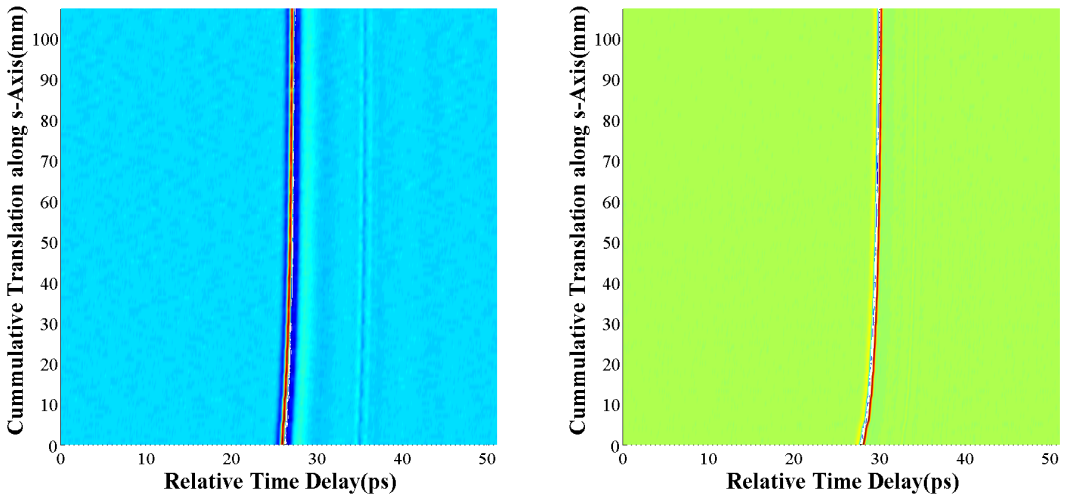

(a) Cylindrical Lens

(b) Waveguide Aperture

Figure 6.4: Transmission Mode - Rapid Scanning Delay Line

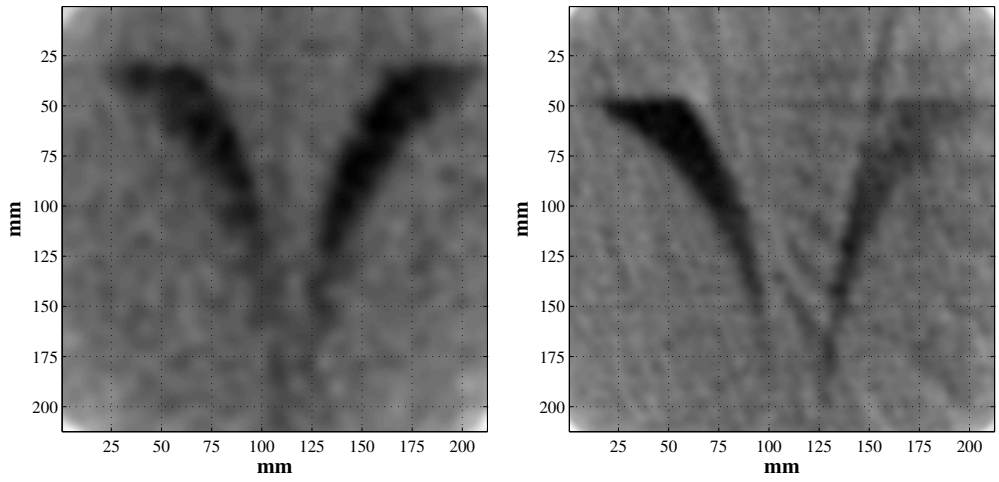

(a) Cylindrical Lens D=0.25 (b) Waveguide Aperture D=0.4

Figure 6.5: Transmission mode reconstruction from peaks - Rapid Scanning Delay Line

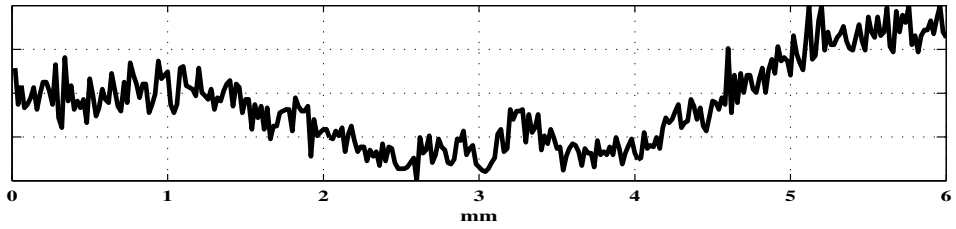

(a) Cylindrical Lens

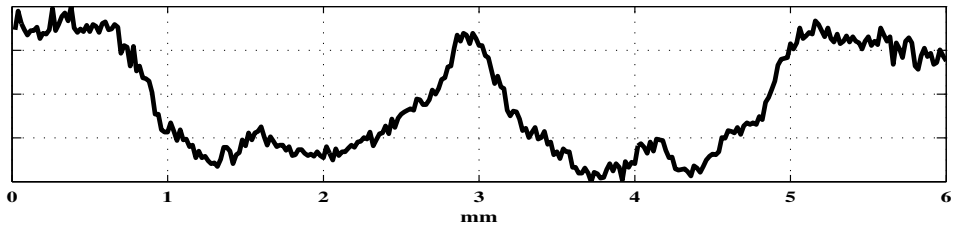

(b) Waveguide Aperture

Figure 6.6: First Projection Angle $\theta = 0^o$, transmission mode - peaks

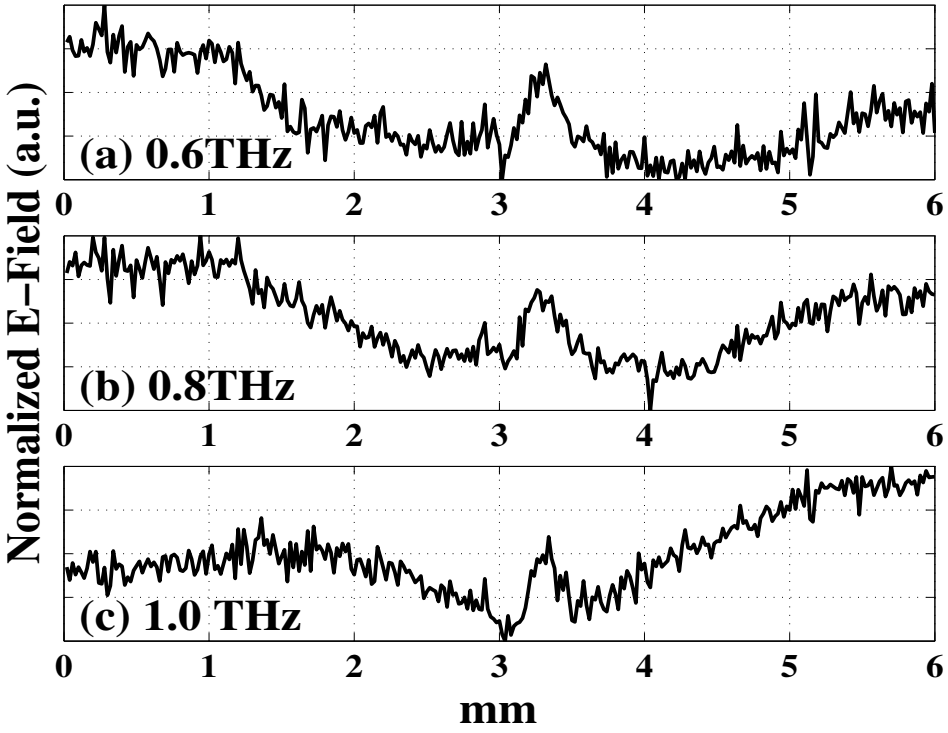

Figure 6.7: First angle $\theta = 0^o$ using cylindrical lens

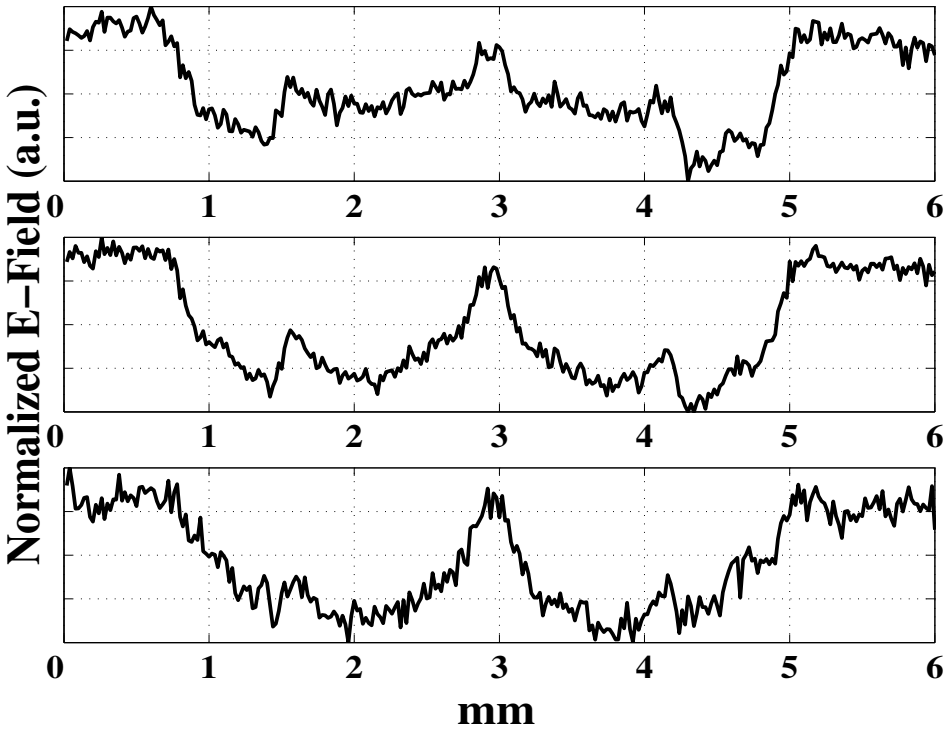

Figure 6.8: First angle $\theta = 0^o$ using waveguide aperture

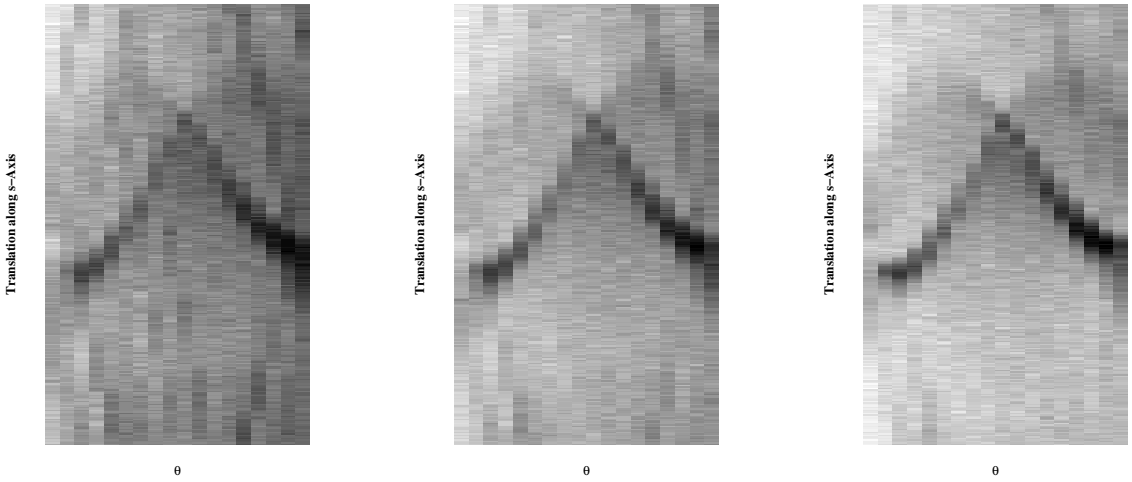

(a) 0.6THz (b) 0.8THz (c) 1.0THz

Figure 6.9: Cylindrical lens data in radon space

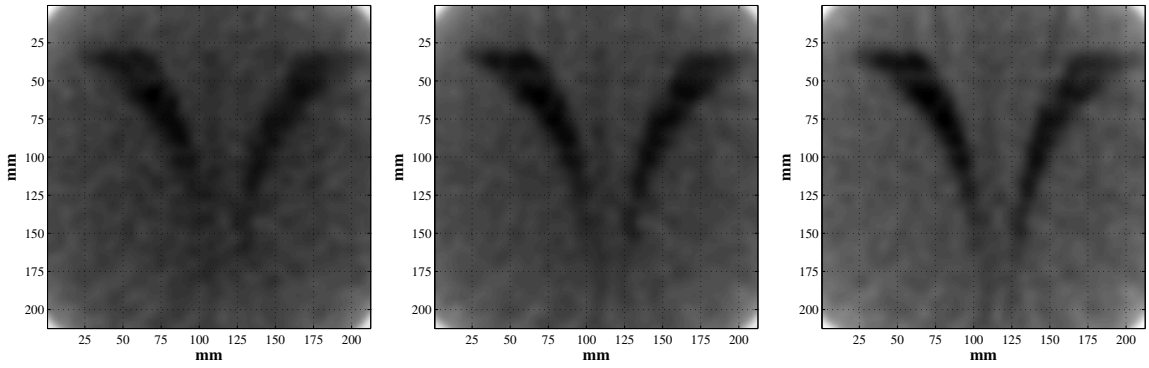

(a) 0.6THz (b) 0.8THz (c) 1.0THz

Figure 6.10: Cylindrical Lens D=0.25

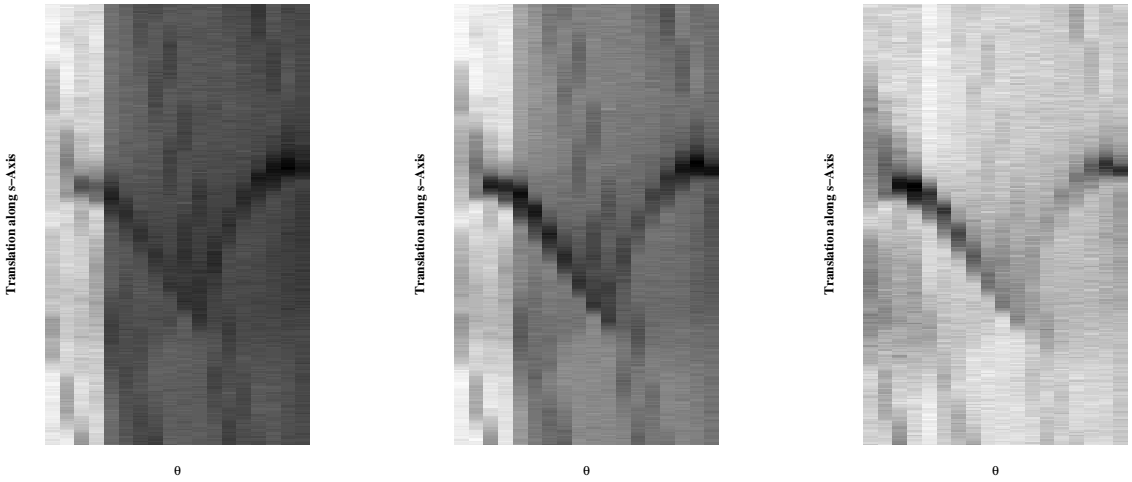

(a) 0.6THz (b) 0.8THz (c) 1.0THz

Figure 6.11: Waveguide aperture data in radon space

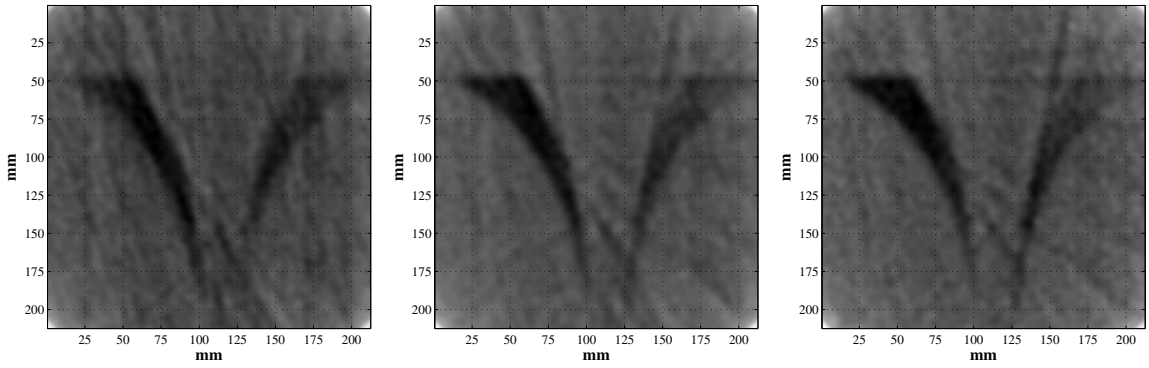

(a) 0.6THz (b) 0.8THz (c) 1.0THz

Figure 6.12: Waveguide Aperture D=0.4

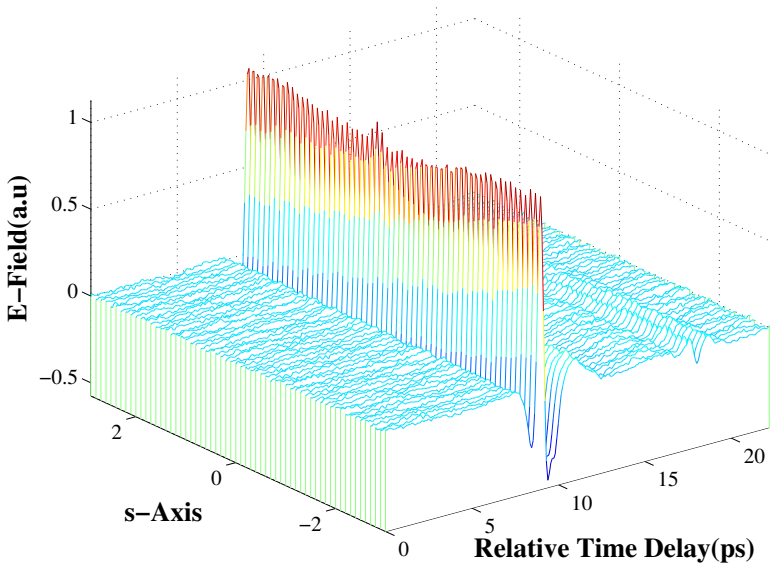

(a) Cylindrical Lens

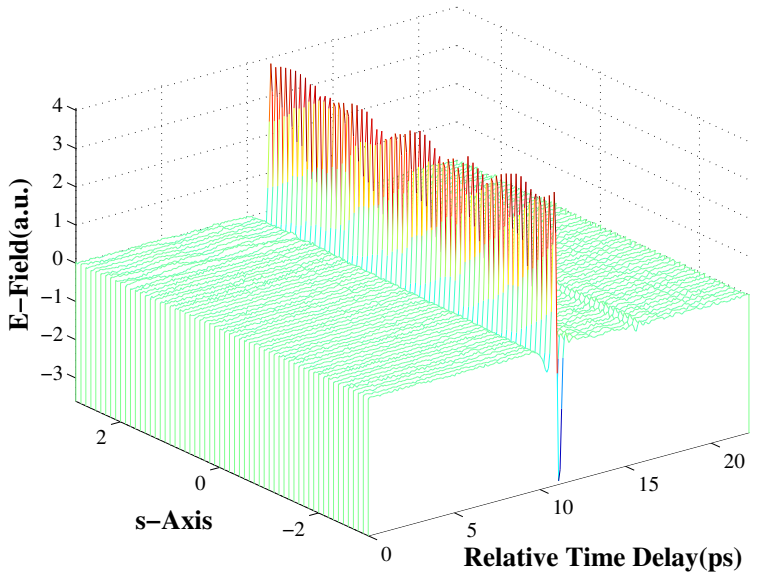

(b) Waveguide Aperture

Figure 6.13: Time resolved data for the first projection angle $\theta = 0$ in transmission mode

6.1.2 Reflection Mode

In reflection mode it was only possible to acquire images using a lock-in amplifier for the waveguide aperture. The rapid scanning delay-line data acquisition method did not yield a sufficient signal-to-noise ratio to be usable. This is mainly due to the low coupling efficiency at the aperture output when compared to the cylindrical lens. It was also necessary to increase the transconductance of the current amplifier when using the waveguide aperture.

Also, a measurement of the F-chip pattern, shown in figure 3.13(a), using the waveguide aperture is presented. This measurement was taken using a lock-in amplifier with a time-constant, τ, equal to 3 seconds.

Lock-in

Figures 6.14(a) and 6.14(b) show the acquired data in radon space for both apertures. As can be seen from the top graph in figure 6.14(c), which shows the first projection angle $\theta = 0^o$, the waveguide aperture clearly resolves more features of the target reflective structure than the cylindrical lens, figure 6.14(c) bottom graph. Both plots in figure 6.14(c) are normalized, and the waveguide plot offset.

Figures 6.15 and 6.16 show the reconstructed images in reflection mode for both apertures, using different filter scaling factors for the filtered backprojection. Comparing figures 6.15(a), 6.15(b) and 6.15(c), the adverse effect of more aggressive filtering on image resolution can be seen.

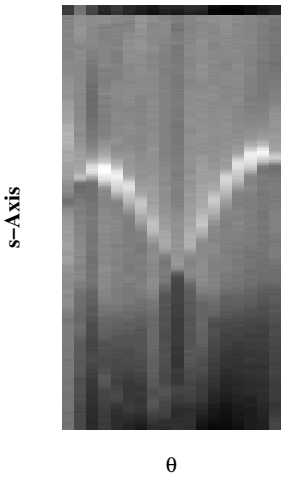

(a) Cylindrical lens

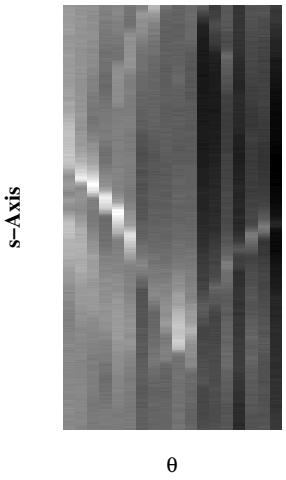

(b) Waveguide aperture

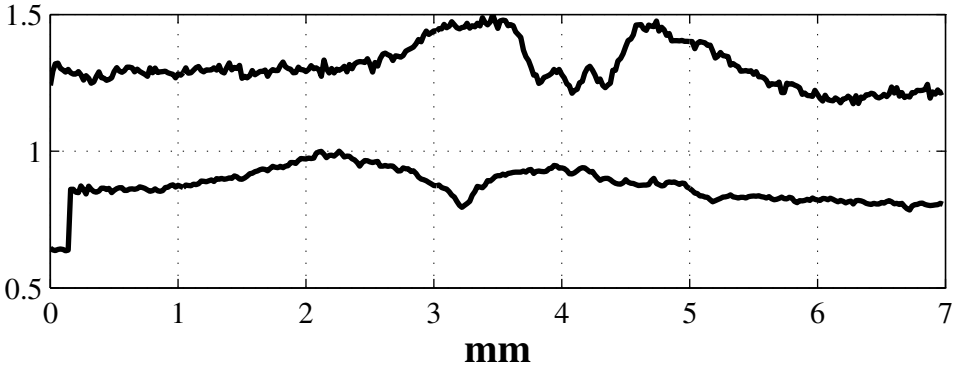

(c) First Projection Angle for waveguide aperture (top) and cylindrical lens (bottom)

Figure 6.14: Raw data in radon space - Reflection

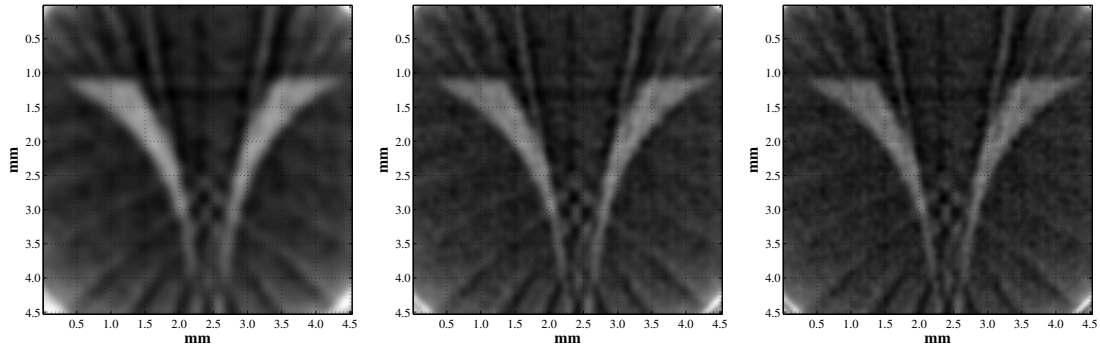

(a) D=0.25 (b) D=0.4 (c) D=0.5

Figure 6.15: Cylindrical Lens aperture reconstruction - Lock-in

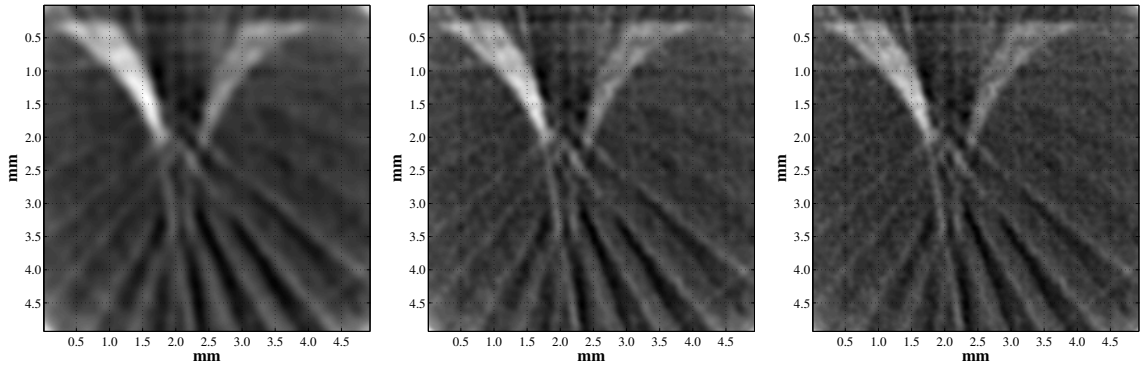

(a) D=0.25 (b) D=0.4 (c) D=0.5

Figure 6.16: Waveguide aperture reconstruction - Lock-in

F-Chip Transmission Line Profile Measurement

A calculation of the effect of the THz beam size on resolution was show in figure 3.13(a). Figure 6.17(bottom) shows a profile measurement of the F-Chip transmission lines using the waveguide aperture. The line-widths are listed in table 3.1. The waveguide aperture is clearly able to resolve transmission lines number five($120\mu m$ gap) and number six($200\mu m$ gap,first from right). Transmission lines one through four cannot be considered resolved. Using the cylindrical lens for this measurement did not resolve any features at all.

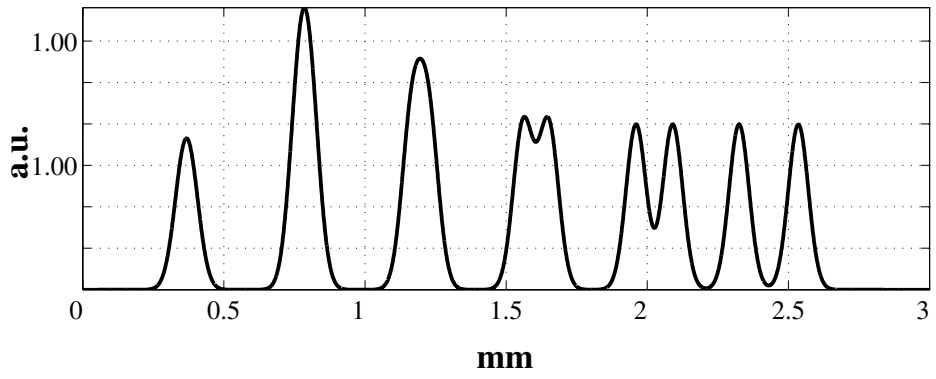

(a) Convolution of F-Chip pattern with $100\mu m$ Gaussian

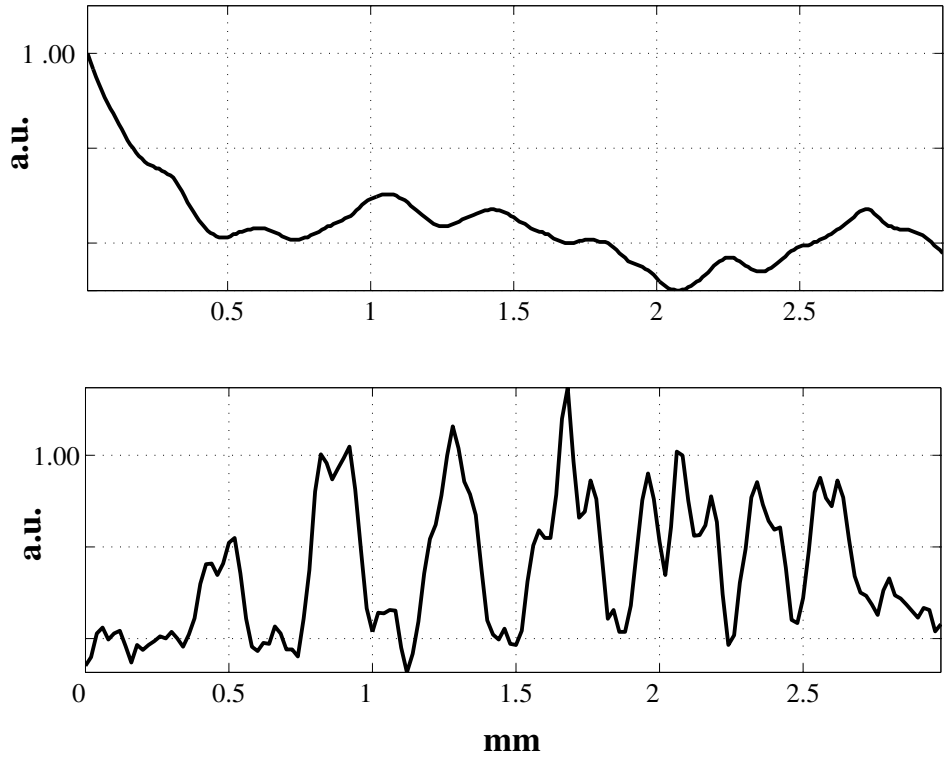

(b) top: Cylindrical lens, bottom:Waveguide Aperture

Figure 6.17: F-Chip measurements

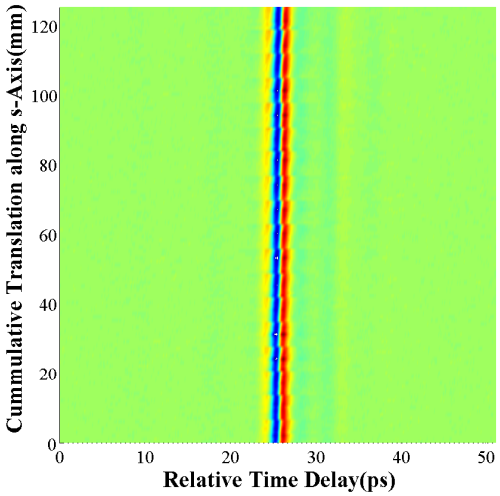

Figure 6.18: Cylindrical lens - Rapid Scanning Delay Line

Rapid Scanning Delay Line - Cylindrical Lens Only

Due to the low SNR of the waveguide aperture measurements, it was not possible to use the rapid scanning delay line. Even the cylindrical lens measurements show a significant increase in noise compared to the lock-in measurement. Figure 6.18 shows all time resolved projection measurements stacked back to back. Figures 6.21 shows the image reconstructed from discrete frequencies.

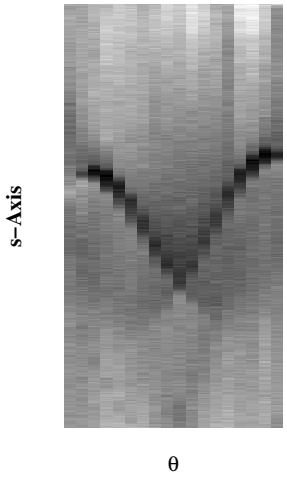

(a) Cylindrical lens

Figure 6.19: Raw data in radon space - Rapid Scanning Delay Line

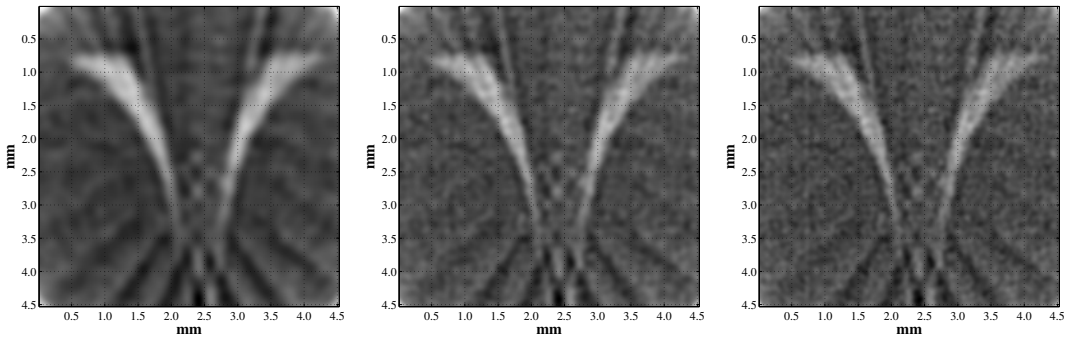

(a) D=0.25 (b) D=0.4 (c) D=0.5

Figure 6.20: Cylindrical Lens aperture reconstruction from peaks - Rapid Scanning Delay Line - from peaks

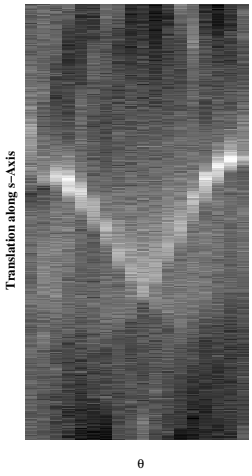

(a) 0.6THz

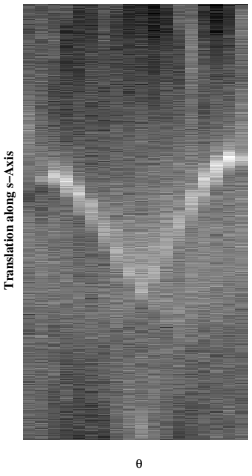

(b) 0.8THz

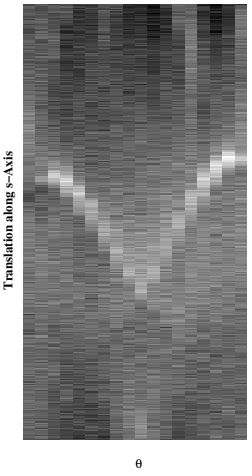

(c) 1.4THz

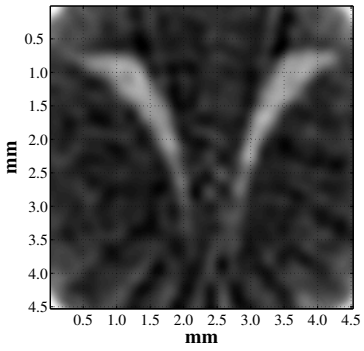

(d) 0.6THz

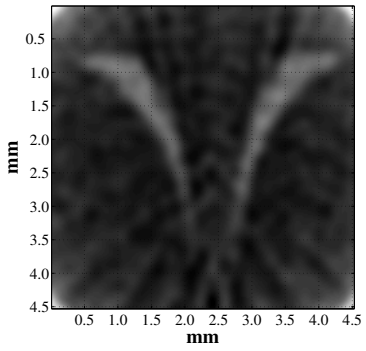

(e) 0.8THz

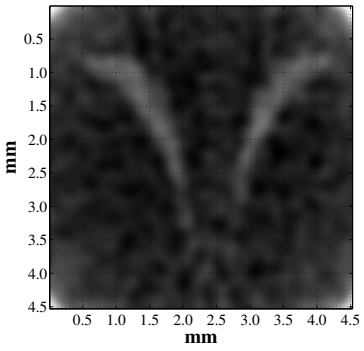

(f) 1.4THz

Figure 6.21: Cylindrical lens - reflection mode - discrete frequencies

6.1.3 Comparison

To compare the results presented, figure 6.22 shows horizontal cross-sectional views of the reconstructed images using a lock-in amplifier for all imaging methods and apertures. The position of the cross-section was chosen as to show the highest resolution achievable for each aperture. The dashed lines in figure 6.22 show the measured distance between the transmission lines:

- 6.22(a): $381\mu m$
- 6.22(b): $213\mu m$
- 6.22(c): $290\mu m$
- 6.22(d): $230\mu m$

The widths of the transmission lines are as follows:

- 6.22(a): $279\mu m$
- 6.22(b): $162\mu m$
- 6.22(c): $218\mu m$
- 6.22(d): $162\mu m$

From the cross-sectional plots and the above line-width measurements it can be seen that in both configurations, the waveguide aperture images shows an increase in resolution compared to the cylindrical lens images. The F-Chip profile measurements shown in figure 6.17 show the increase in resolution, where the cylindrical lens did not resolve any transmission lines at all compared to the parallel plate waveguide.

6.2 Conclusion

This work demonstrated a new imaging technique in the THz frequency regime using both conventional optics and the near-field properties of a parallel-plate waveguide as

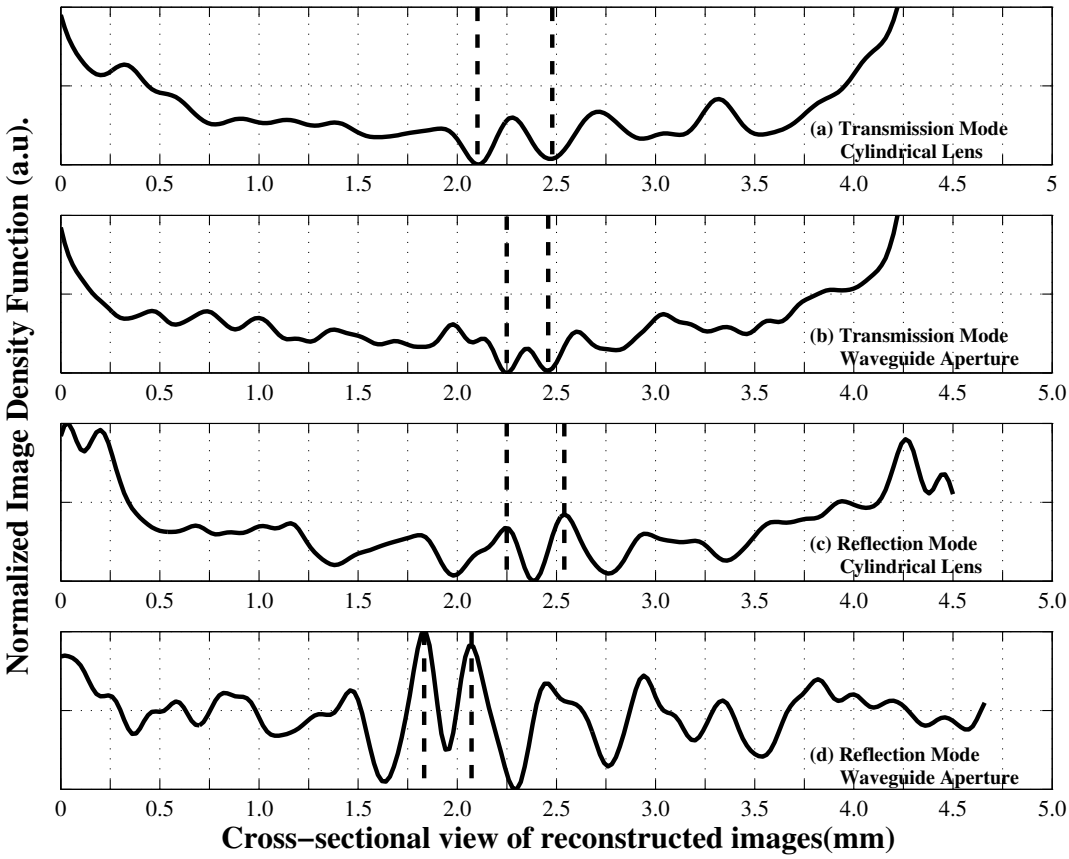

Figure 6.22: Cross-sectional views for both apertures in both geometries

an imaging aperture. These apertures were used in two imaging geometries, transmission and reflection. It was shown that the parallel plate waveguide aperture allows for imaging at sub-wavelength resolution. Figure 6.22 shows a comparison of the resolution for both the cylindrical lens, and waveguide aperture. The waveguide aperture is able to resolve features as small as $120\mu m$, figure 6.17. Also two different methods of data acquisition were used to collect the image data. The rapid scanning delay line method allows for fully time resolved scans from which it might be possible to extract further information about the target, however the amount of data acquired is rather large. The lock-in detection method allows for a convenient way to acquire enough

data to reconstruct the image, at slightly faster speeds than the rapid scanning delay line method.

Coupled with a waveguide integrated THz generation and detection scheme, this type of imaging technique can be used to develop a handheld reflection-imaging probe, which depending on the type of detection employed may or may not need reconstruction techniques. Full mobility of the handheld probe can be achieved by fiber coupling the transmitter and receiver. Also, using a more powerful THz transmitter, it should be possible to obtain better results without the use of a lock-in amplifier, while at the same time retaining full time resolved measurements of the image. A possible extension of this work might be the development of an imaging technique where resolution along the aperture is maintained. This can be accomplished using a linear detector array, instead of a single dipole. An imaging probe of this kind would be able to image a target in a single linear scan, and also provide depth information from reflection from boundaries within the target, while at the same time maintaining higher resolution, without the need of reconstruction algorithms. A THz handheld probe of this kind might used in non-destructive testing of materials during manufacturing or the medical field for example. Several studies have been published on using THz radiation to detect and identify skin cancer [14, 15, 39, 40, 41] and this type of imaging method would provide the necessary resolution and portability to be used as a diagnostic tool.

Bibliography

[1] Tae-In Jeon and D. Grischkowsky. Characterization of optically dense, doped semiconductors by reflection THz time domain spectroscopy. *APPLIED PHYSICS LETTERS*, 72(23):3332–3334, 1998.

[2] Tae-In. Jeon and D. Grischkowsky. Electrical characterization of conducting polypyrrole by THz time-domain spectroscopy. *APPLIED PHYSICS LETTERS*, 77(16):2452–2454, 2000.

[3] R. Sprik, Duling I.N., C.-C. Chi, and D. Grischkowsky. Far infrared spectropscopy with subpicosecond electrical pulses on transmission lines. *APPLIED PHYSICS LETTERS*, 51(7):548–550, 1987.

[4] M. van Exter, Ch. Fattinger, and D. Grischkowsky. Terahertz time-domain spectroscopy of water vapor. *OPTICS LETTERS*, 14(20):1128–1130, 1989.

[5] D. Grischkowsky, S. Keiding, M. van Exter, and Ch. Fattinger. Far-infrared time-domain spectroscopy with terahertz beams of dielectrics and semiconductors. *JOURNAL OF THE OPTICAL SOCIETY OF AMERICA B*, 7(10):2006–2015, 1990.

[6] B.N. Flanders, R.A. Cheville, D. Grischkowsky, and N.F. Scherer. Pulsed terahertz transmission spectroscopy of liquid $CHCl_3$, CCl_4, and their mixtures. *JOURNAL PF PHYSICAL CHEMISTRY*, 100:11824–11835, 1996.

[7] B. B. Hu and M. C. Nuss. Imaging with terahertz waves. *Optics Letters*, 20(16):1716–&, 1995.

[8] J. O'Hara and D. Grischkowsky. Quasi-optic terahertz imaging. *OPTICS LETTERS*, 26(23):1918–1920, 2001.

[9] K. McClatchey, M.T. Reiten, and R.A. Cheville. Time resolved synthetic aperture terahertz impulse imaging. *APPLIED PHYSICS LETTERS*, 79(27):4485–4487, 2001.

[10] S.A. Harmon and R.A. Cheville. Part-per-million gas detection from long-baseline THz spectroscopy. *APPLIED PHYSICS LETTERS*, 85(11):2128–2130, 2004.

[11] R.A. Cheville and D. Grischkowsky. Time domain terahertz impulse ranging studies. *APPLIED PHYSICS LETTERS*, 67(14):1960–1962, 1995.

[12] R.A. Cheville, R.W. McGowan, and D. Grischkowsky. Late-time target response measured with terahertz impulse ranging. *IEEE TRANSACTIONS ON ANTENNAS AND PROPAGATION*, 45(10):1518–1524, 1997.

[13] E Pickwell, BE Cole, AJ Fitzgerald, VP Wallace, and M Pepper. Simulation of terahertz pulse propagation in biological systems. *APPLIED PHYSICS LETTERS*, 84(12):2190–2192, 2004.

[14] RM Woodward, BE Cole, VP Wallace, RJ Pye, DD Arnone, EH Linfield, and M Pepper. Terahertz pulse imaging in reflection geometry of human skin cancer

and skin tissue. *PHYSICS IN MEDICINE AND BIOLOGY*, 47(21):3853–3863, 2002.

[15] RM Woodward, VP Wallace, DD Arnone, EH Linfield, and M Pepper. Terahertz pulsed imaging of skin cancer in the time and frequency domain. *JOURNAL OF BIOLOGICAL PHYSICS*, 29(2-3):257–261, 2003.

[16] DM Mittleman, S Hunsche, L Boivin, and MC Nuss. T-ray tomography. *OPTICS LETTERS*, 22(12):904–906, 1997.

[17] S Hunsche, M Koch, I Brener, and MC Nuss. THz near-field imaging. *OPTICS COMMUNICATIONS*, 150(1-6):22–26, 1998.

[18] HT Chen, R Kersting, and GC Cho. Terahertz imaging with nanometer resolution. *APPLIED PHYSICS LETTERS*, 83(15):3009–3011, 2003.

[19] J Bae, T Okamoto, T Fujii, K Mizuno, and T Nozokido. Experimental demonstration for scanning near-field optical microscopy using a metal micro-slit probe at millimeter wavelengths. *APPLIED PHYSICS LETTERS*, 71(24):3581–3583, 1997.

[20] T Nozokido, J Bae, and K Mizuno. Scanning near-field millimeter-wave microscopy using a metal slit as a scanning probe. *IEEE TRANSACTIONS ON MICROWAVE THEORY AND TECHNIQUES*, 49(3):491–499, 2001.

[21] M. Vanexter and D. R. Grischkowsky. Characterization of an optoelectronic terahertz beam system. *IEEE TRANSACTIONS ON MICROWAVE THEORY AND TECHNIQUES*, 38(11):1684–1691, 1990.

[22] M. Vanexter, Ch. Fattinger, and D. R. Grischkowsky. Terahertz time-domain spectroscopy of water vapor. *OPTICS LETTERS*, 14(20):1128–1130, 1989.

[23] D KROKEL, D GRISCHKOWSKY, and MB KETCHEN. Subpicosecond electrical pulse generation using photoconductive switches with long carrier lifetimes. *APPLIED PHYSICS LETTERS*, 54(11), 1989.

[24] P.Uhd Jepsen, R.H. Jacobsen, and S.R. Keiding. Generation and detection of terahertz pulses from biased semiconductor antennas. *JOURNAL OF THE OPTICAL SOCIETY OF AMERICA B*, 13(11):2424–2436, 1996.

[25] C Chi F Doany, D Grischkowsky and. Carrier lifetime versus ion-implantation dose in silicon on sapphire. *Applied Physics Letters*, 50(8):460–462, 1987.

[26] P.Uhd Jepsen and S.R. Keiding. Radation patterns from lens-coupled terahertz antennas. *OPTICS LETTERS*, 20(8):807–809, 1995.

[27] MT Reiten, SA Harmon, and RA Cheville. Terahertz beam propagation measured through three-dimensional amplitude profile determination. *JOURNAL OF THE OPTICAL SOCIETY OF AMERICA B-OPTICAL PHYSICS*, 20(10):2215–2225, 2003.

[28] G Massey. Microscopy and pattern generation with scanned evanescent waves. *Applied Optics*, 23(5):658–660, 1984.

[29] R Mendis and D Grischkowsky. Undistorted guided-wave propagation of subpicosecond terahertz pulses. *OPTICS LETTERS*, 26(11):846–848, 2001.

[30] Constantine A. Balanis. *Advanced engineering electromagnetics*. Wiley, New York, 1989.

[31] Joseph W. Goodman. *Introduction to Fourier optics*. McGraw-Hill series in electrical and computer engineering. McGraw-Hill, New York, 2nd edition, 1996.

[32] K. Hongo, Y. Ogawa, T. Itoh, and K. Ogusu. Field distribution in a flanged parallel-plate waveguide. *IEEE Transactions on Antennas and Propagation*, 23(4):558–560, 1975.

[33] Eugene Hecht. *Optics 4th ed.* Addison Wesley, 2002.

[34] Stanley R. Deans. *The Radon transform and some of its applications*. Wiley, New York, 1983.

[35] Anil K. Jain. *Fundamentals of digital image processing*. Prentice Hall, Englewood Cliffs, NJ, 1989.

[36] Allen Taflove. *Computational Electrodynamics:The Finite-Difference Time-Domain Method*. Artech House, Boston, 1st edition, 1995.

[37] Mathew N.O. Sadiku. *Numerical Techniques in Electromagnetics*. CRC Press, Boca Raton, 2nd edition, 2001.

[38] J Earl Jones, L Tsai, RC Rudduck, CT Swift, and WD Burnside. The admittance of a parallel-plate waveguide aperture illuminating a metal sheet. *IEEE TRANSACTIONS ON ANTENNAS AND PROPAGATION*, AP-16(5):528–353, 1968.

[39] RM Woodward, VP Wallace, RJ Pye, BE Cole, DD Arnone, EH Linfield, and M Pepper. Terahertz pulse imaging of ex vivo basal cell carcinoma. *JOURNAL OF INVESTIGATIVE DERMATOLOGY*, 120(1):72–78, 2003.

[40] VP Wallace, AJ Fitzgerald, S Shankar, N Flanagan, R Pye, J Cluff, and DD Arnone. Terahertz pulsed imaging of basal cell carcinoma ex vivo and in vivo. *BRITISH JOURNAL OF DERMATOLOGY*, 151(2):424–432, 2004.

[41] E Pickwell, BE Cole, AJ Fitzgerald, M Pepper, and VP Wallace. In vivo study of human skin using pulsed terahertz radiation. *PHYSICS IN MEDICINE AND BIOLOGY*, 49(9):1595–1607, 2004.

VITA

Mohammad Ma'moun Awad

Candidate for the Degree of

Master of Science

Thesis: TERAHERTZ IMAGING FROM PROJECTIONS USING A PARALLEL PLATE WAVEGUIDE APERTURE IN TRANSMISSION AND REFLECTION MODE

Major Field: Electrical Engineering

Biographical:

Personal Data: Born in Geldern, NRW Germany, On November 27 1976

Educational: Received Bachelor of Science degree in Electrical and Computer Engineering from Oklahoma State University in May 2001. Completed the requirements for the Masters of Science degree with a major in Electrical Engineering in May 2005.

Experience: As an undergraduate worked as a teaching assistant and lab instructor for several electrical engineering courses (Jan. 1999-May 2001). As graduate worked as a research assistant at Oklahoma State University's Ultrafast Terahertz Optoelectronics Laboratory (June 2001-May2005).

Name: Mohammad Ma'moun Awad Date of Degree: May 2005

Institution: Oklahoma State University Location: Stillwater, Oklahoma

Title of Study: TERAHERTZ IMAGING FROM PROJECTIONS USING A PARALLEL PLATE WAVEGUIDE APERTURE IN TRANSMISSION AND REFLECTION MODE

Pages in Study: 84 Candidate for the Degree of Master of Science

Major Field: Electrical Engineering

Scope of Study:

Imaging resolution at terahertz frequencies is limited by the diffraction limit of the optics where the focus spot size is approximately on the order of a wavelength. We demonstrate a novel imaging technique that achieves sub-wavelength resolution at terahertz frequencies. A parallel plate terahertz waveguide is used as a near field imaging aperture in a transmission and reflection geometry. The image data is collected as projections of the target and are in the form of a radon transform. A reconstruction algorithm has to be used to extract the image from those projections. This type of reconstruction is similar to reconstruction techniques used in X-ray computed tomography (CT).

Findings and Conclusions:

Using the near-field characteristics of the parallel plate waveguide, was possible to acquire images with sub-wavelength resolution. These images were then compared to images acquired using conventional diffraction limited optics and showed an increase in resolution in both transmission and reflection geometries. The highest achievable resolution was determined by the plate spacing of the parallel plate waveguide.

Advisor's Approval _____Alan Cheville_____